

1 **PETROLOGY OF BLUESCHIST FROM THE WESTERN HIMALAYA (LADAKH, NW INDIA):**  
2 **EXPLORING THE COMPLEX BEHAVIOUR OF A LAWSONITE-BEARING SYSTEM IN A**  
3 **PALAEO-ACCRETIONARY SETTING**

4  
5  
6  
7 Chiara Groppo<sup>a,b</sup>, Franco Rolfo<sup>a,b</sup>, Himanshu K. Sachan<sup>c</sup>, Santosh K. Rai<sup>c</sup>

8  
9  
10  
11 a - Department of Earth Sciences, University of Torino, Via Valperga Caluso 35, Torino, 10125, Italy

12 b - IGG-CNR, Via Valperga Caluso 35, Torino, 10125, Italy

13 c - Wadia Institute of Himalayan Geology, Dehra Dun, 248001, India

14  
15  
16 Corresponding Author

17 Chiara Groppo

18 Dept. of Earth Sciences, University of Torino

19 Via Valperga Caluso, 35 – 10125 Torino, Italy

20 Tel. +39 0116705106

21 Fax +39 0116705128

22 E-mail: [chiara.groppo@unito.it](mailto:chiara.groppo@unito.it)

23

## 24 **1. Introduction**

25 Lawsonite-bearing blueschists and eclogites are witnesses of cold subduction processes occurred along  
26 ancient convergent margins. Metamorphic processes involved in the generation and preservation of  
27 lawsonite are crucial in many research areas, ranging from petrology to geochemistry, geodynamics and  
28 geophysics (e.g. Hacker et al., 2003; Bebout, 2007; Hacker, 2008; Davis, 2011; Martin et al., 2011; Vitale  
29 Brovarone et al., 2011; Chantel et al., 2012; Abers et al., 2013; Cao et al., 2013; Kim et al., 2013; Spandler &  
30 Pirard, 2013). Therefore, lawsonite-bearing eclogites and, to a lesser extent, lawsonite-bearing blueschists  
31 have been the focus of several studies, especially in recent years (Tsujimori and Ernst, 2014 and references  
32 therein). Compared to the rare occurrences of lawsonite eclogites worldwide (see the review paper by  
33 Tsujimori et al., 2006), lawsonite blueschist units are reported from several orogenic belts (e.g. Agard et al.,  
34 2009; Tsujimori and Ernst, 2014 and references therein); however, in many cases, the lawsonite blueschist-  
35 facies assemblages formed at peak metamorphic conditions are widely overprinted by epidote blueschist-  
36 and/or greenschist-facies retrograde assemblages during exhumation (e.g. Ernst, 1988; Agard et al., 2001,  
37 2006; Jolivet et al., 2003; Schumacher et al., 2008; Plunder et al., 2012). Lawsonite preservation requires  
38 exhumation along cold geothermal gradients, comparable to those required for its formation during  
39 subduction. Such geothermal regimes are typical of ancient Pacific-type plate convergent margins (see  
40 Tsujimori and Ernst, 2014 for a review); the occurrence of well-preserved high-pressure lawsonite  
41 blueschists and eclogites in an orogenic belt is therefore an appealing clue of a peculiar tectonic setting.

42 Although the Himalaya is the archetype of collisional orogens, formed as a consequence of the closure of  
43 the Tethyan ocean separating India from Asia followed by continental collision between the two plates,  
44 high-pressure metamorphic rocks are rare along the orogen (e.g. Lombardo and Rolfo, 2002; Guillot et al.,  
45 2008). Moreover, most of the eclogites reported so far from the Himalaya correspond to the  
46 metamorphosed continental Indian crust dragged below Asia (NW Himalaya: Kaghan, Tso Morari and Stak  
47 massifs; Pognante and Spencer, 1991; Guillot et al., 1997, 1999, 2007, 2008; de Sigoyer et al., 2000; O'Brien  
48 et al., 2001; Sachan et al., 2004; Lanari et al., 2013), or underthrust beneath southern Tibet (E Himalaya:  
49 Kharta and Bhutan; Lombardo and Rolfo, 2002; Groppo et al., 2007; Chakungal et al., 2010; Grujic et al.,  
50 2011; Warren et al., 2011). Evidence of the ancient Tethyan oceanic crust subducted below Asia are also  
51 rare and locally occur within the Indus-Tsangpo Suture (ITS) zone, which separates the northern margin of  
52 the Indian plate to the south (i.e. the Himalaya s.s.) from the southern margin of the Asian plate to the  
53 north (represented, from west to east, by the Kohistan Arc, the Ladakh block and the Lhasa block). These  
54 evidences are: (i) few lawsonite blueschists from the western part of the ITS zone in Pakistan (Shangla:  
55 Shams, 1972; Frank et al., 1977) and Ladakh (NW India) (Sapi-Shergol: Honegger et al., 1989; Zildat: Viridi et  
56 al., 1977; de Sigoyer et al., 2004), interpreted as related to paleo-accretionary prisms formed in response to  
57 the subduction of the Neo-Tethyan ocean below the Asian plate (e.g. Robertson, 2000; Mahéo et al., 2006;  
58 Guillot et al., 2008); (ii) few eclogite, lawsonite- and epidote blueschist -facies rocks reported from the  
59 Indo-Burmese Ranges (Nagaland Ophiolite Complex: Ghose and Singh, 1980; Acharyya, 1986; Chatterjee  
60 and Ghose, 2010; Ao and Bhowmik, 2014; Bhowmik and Ao, 2015; Chin Hill Ophiolite: Socquet et al., 2002),  
61 interpreted as the eastern extension of the ITS zone. These rare high-pressure/low-temperature (HP-LT)  
62 rocks are therefore crucial for constraining the evolution of the India-Asia convergence zone during the  
63 closure of the Neo-Tethyan ocean (Guillot et al., 2008); in this framework, the detailed reconstruction of  
64 their P-T paths is a fundamental step toward a reliable geodynamic interpretation.

65 The P-T evolution of the eclogites and blueschists from the Indo-Burmese Ranges has been recently  
66 constrained by means of modern petrological methods (e.g. pseudosections); variable peak P-T conditions  
67 have been reported from different portions of the suture zone, ranging from ~340 °C, ~11.5 kbar (lawsonite  
68 blueschists: Ao and Bhowmik, 2014) to 540 ± 35 °C, 14.4 ± 2 kbar (epidote blueschists: Bhowmik and Ao,

69 2015) to 580-610°C and 17-20 kbar (eclogites: Chatterjee and Ghose, 2010). On the opposite, modern  
70 petrologic studies aimed at constraining the P-T evolution of the blueschist-facies rocks from the western  
71 sector of the ITS zone are lacking. Some 25 years ago, Honegger et al. (1989) reported peak metamorphic  
72 conditions of 350-420 °C, 9-11 kbar for the Sapi-Shergol lawsonite blueschists using conventional  
73 thermobarometry. P-T estimates for the Shangla blueschists were published even earlier (Guiraud, 1982;  
74 Jan, 1985) and suggest peak P-T conditions of ca. 400 °C, 5 kbar. Although detailed, these petrological  
75 studies are based on conventional methods and need to be updated using more recent and powerful  
76 petrological approaches (e.g. isochemical phase diagrams).

77 In this paper, the lawsonite blueschists from Sapi-Shergol have been petrologically re-investigated with the  
78 aims of: (i) constraining their P-T evolution; (ii) evaluating the influence of Fe<sub>2</sub>O<sub>3</sub> and of H<sub>2</sub>O on the stability  
79 of the high pressure mineral assemblages; (iii) understanding the processes controlling lawsonite formation  
80 and preservation, and (iv) interpreting the P-T evolution of the Sapi-Shergol blueschists in the framework of  
81 India-Asia collision.

82

## 83 **2. Geological setting**

84 In the India–Asia convergence system, the ITS zone records the closure of the Neo-Tethyan ocean from Late  
85 Cretaceous to Tertiary time (Frank et al., 1977; Honegger et al., 1989; Cannat and Mascle, 1990). Among  
86 the few occurrences of high-pressure rocks along the ITS, those of Ladakh (NW India) are the best in terms  
87 of rock freshness, areal extent and metamorphic assemblages. Blueschists in the Ladakh area occur along  
88 the ITS in few localities: from SE to NW these are Puga, Urtsi, Hinju and Sapi-Shergol (Honegger et al.,  
89 1989). The largest outcrop is that of Sapi-Shergol (35 km south of Kargil), where the blueschists form a 12  
90 km x 1 km E-W trending narrow zone.

91 Tectonically, the Sapi-Shergol blueschists belong to a narrow belt called “Ophiolitic Mélange Unit”  
92 (Honegger et al., 1989) (Fig. 1), which outcrops over a distance of 250 km along the ITS suture. This belt  
93 consists of several thrust slices sandwiched between the Nindam-Naktul-Dras nappes to the north, and the  
94 Lamayuru-Karamba nappes to the south. The Ophiolitic Mélange Unit is interpreted as a relic of a paleo-  
95 accretionary prism formed in response to the northward subduction of the Neo-Tethyan ocean, originally  
96 separating the Ladakh arc to the south from the southern Asian active margin to the north (Mahéo et al.,  
97 2006). This paleo-accretionary prism consists of sedimentary units including blocks of (mainly) basic  
98 lithologies that have been metamorphosed under variable P-T conditions, ranging from low-grade  
99 metamorphism to lawsonite blueschist -facies metamorphism (Frank et al., 1977; Honegger et al., 1989;  
100 Jan, 1987; Reuber et al., 1987; Sutre, 1990; Ahmad et al., 1996; Robertson, 2000; Mahéo et al., 2006).

101 The Sapi-Shergol Ophiolitic Mélange (SSOM) is a complex unit which includes slices of the paleo-  
102 accretionary prism, intercalated with numerous slices of other units including the Nindam and Lamayuru  
103 turbidites and low grade meta-ophiolitic slices consisting of serpentinitized peridotites intruded by basic  
104 dikes (“sheared serpentinites” of Robertson, 2000). The narrow blueschist zone cropping out close to the  
105 village of Shergol (Fig. 1, 2a) is overlain discordantly by the Shergol conglomerate of post-Eocene (Oligo-  
106 Miocene?) age (Honegger et al., 1989). Blueschist lithologies are dominated by volcanoclastic sequences of  
107 basic material (Fig. 2b,c) with subordinate interbedding of cherts and minor carbonatic lithologies. Mahéo  
108 et al. (2006) suggested that the blueschists derive from calc-alkaline igneous rocks formed in an intra-  
109 oceanic arc environment. K-Ar ages of whole-rocks and glaucophane suggest an age of ca. 100 Ma for the  
110 high-pressure metamorphism (Honegger et al., 1989).

111

### 112 **2.1 Main blueschist lithologies of the SSOM**

113 Metabasic and metavolcanoclastic rocks are the dominant lithologies in the SSOM, and they are associated  
114 to subordinate interbedded metasediments. These lithologies have been described in detail by Honegger et  
115 al. (1989); the most relevant petrographic features are therefore only summarized here.

116

#### 117 *2.1.1 Metabasic and metavolcanoclastic rocks*

118 Metabasic rocks are mainly represented by fine-grained glaucophane-bearing schists (Fig. 2c,e) with  
119 variable amounts of lawsonite and minor clinopyroxene and phengite. Lawsonite can be either fine-grained  
120 or porphyroblastic and it generally overgrows the main foliation defined by the alignment of glaucophane ±  
121 phengite (Fig. 2e); where present, phengite often shows a slightly greenish pleochroism. Clinopyroxene  
122 (omphacite/aegirine-augite) generally occurs as fine-grained dusty and fibrous aggregates, probably  
123 replacing former magmatic clinopyroxene fenocrysts. Fine-grained titanite aggregates are often aligned to  
124 the main foliation (Fig. 2e); opaque minerals can be locally abundant and surrounded by pressure fringes of  
125 albite. Locally, remnants of a strongly vesiculated structure are evidenced by the alignment of fine-grained  
126 titanite.

127 Metavolcanoclastic rocks are characterized by a clastic structure and consist of irregular fragments of  
128 metabasic rocks set in a very fine-grained matrix (Fig. 2b). Clasts of metabasic rocks are either rounded or  
129 sharp and vary in size from few millimeters to several centimeters (Fig. 2b, d). The clasts generally consist  
130 of blue amphibole + lawsonite ± minor clinopyroxene in different modal abundances and with different  
131 grain-size (Fig. 2d). The matrix is generally very fine-grained and mainly consists of blue amphibole, green  
132 clinopyroxene (aegirine/omphacite) forming fine-grained dusty aggregates, porphyroblastic lawsonite and  
133 minor phengite and chlorite. Fine-grained aggregates of titanite (leucoxene) replace former ilmenite.

134 Both metabasic rocks and metavolcanoclastic rocks can be crosscut by glaucophane veins and/or late albite  
135 ± calcite, and albite + chlorite ± quartz veins.

136

#### 137 *2.1.2 Metasediments*

138 Both silicic and impure carbonatic metasediments occur as intercalations in the metabasic and  
139 metavolcanoclastic rocks. Among the silicic metasediments, glaucophane + lawsonite + phengite ± garnet  
140 schists, lawsonite + glaucophane + phengite + garnet quartzitic-micaschists and glaucophane + garnet +  
141 phengite quartzites (Fig. 2f) are the most common types. Lawsonite and garnet can be either fine-grained  
142 or porphyroblastic. Lawsonite and garnet porphyroblasts can reach few centimeters and few millimeters in  
143 size, respectively, and generally overgrow the main foliation; lawsonite porphyroblasts are locally dusty due  
144 to the presence of abundant fluid inclusions. Glaucophane and phengite are always fine-grained and define  
145 the main foliation, which is often intensely crenulated. Titanite is ubiquitous as accessory mineral. The  
146 lawsonite blueschists investigated in detail in this paper belong to this group of metasediments.

147 The impure carbonatic metasediments are very fine-grained and mainly consist of lawsonite, calcite,  
148 glaucophane and minor phengite ± prehnite (Fig. 2g). Calcite often occurs as large poikiloblasts including  
149 idioblastic lawsonite. Prehnite is rare and occurs as reniform globular aggregates of fine-grained brownish  
150 fibrous crystals.

151 Late quartz, albite ± quartz and calcite ± albite veins crosscut the main schistosity in most metasediments.

152

### 153 **3. Methods**

#### 154 **3.1 Micro-X-ray fluorescence ( $\mu$ -XRF) maps**

155 The micro-XRF maps of the whole thin sections (Fig. 3 and Fig. SM1, SM2) were acquired using a  $\mu$ -XRF  
156 Eagle III-XPL spectrometer equipped with an EDS Si(Li) detector and with an Edax Vision32 microanalytical  
157 system (Department of Earth Sciences, University of Torino, Italy). The operating conditions were as

158 follows: 100 ms counting time, 40 kV accelerating voltage and a probe current of 900  $\mu$ A. A spatial  
159 resolution of about 65  $\mu$ m in both x and y directions was used. Quantitative modal percentages of each  
160 mineral were obtained by processing the  $\mu$ -XRF maps with the software program “Petromod” (Cossio et al.  
161 2002).

162

### 163 **3.2 Mineral chemistry**

164 Minerals were analysed with a Cambridge Stereoscan 360 SEM equipped with an EDS Energy 200 and a  
165 Pentafet detector (Oxford Instruments) at the Department of Earth Sciences, University of Torino. The  
166 operating conditions were as follows: 50 s counting time and 15 kV accelerating voltage. SEM–EDS  
167 quantitative data (spot size = 2  $\mu$ m) were acquired and processed using the Microanalysis Suite Issue 12,  
168 INCA Suite version 4.01; natural mineral standards were used to calibrate the raw data; the  $\rho\phi Z$  correction  
169 (Pouchou and Pichoir, 1988) was applied. Absolute error is 1  $\sigma$  for all calculated oxides.

170 Mineral chemical data of representative minerals are reported in Tables SM1, SM2. Structural formulae  
171 have been calculated on the basis of 12 oxygens for garnet, 6 oxygens for omphacite, 8 oxygens for  
172 lawsonite, 11 oxygens for phengite and 23 oxygens for amphibole. Fe<sup>+3</sup> has been calculated by  
173 stoichiometry except for amphibole (average Fe<sup>+3</sup> values).

174

### 175 **3.3 Phase diagrams computation**

176 Isochemical phase diagrams were calculated in the MnNKCFMASH(O) system using Perple\_X (version 6.7.1,  
177 Connolly 1990, 2009) and the thermodynamic dataset and equation of state for H<sub>2</sub>O–CO<sub>2</sub> fluid of Holland  
178 and Powell (1998, revised 2004). The following solid solution models were used: garnet (Holland and  
179 Powell, 1998), amphibole (Diener et al., 2007, 2012), omphacite (Green et al., 2007; Diener et al., 2012),  
180 chlorite (Holland et al., 1998), phengite (Holland and Powell, 1998), plagioclase (Newton et al., 1980) and  
181 epidote (Holland and Powell, 1998). Quartz, lawsonite, and zoisite were considered as pure end-members.  
182 The bulk rock compositions of the studied samples have been calculated by combining the mineral  
183 proportions obtained from the modal estimate of micro-XRF maps (Fig. 3, Table 1) with mineral chemistry  
184 acquired at SEM–EDS, and are reported in Table 1: these whole rock compositions have been used to  
185 model: (i) the whole prograde P-T evolution in sample 14-4B; (ii) the growth of garnet core + mantle in  
186 sample 14-6F. For this last sample, the possible effects of chemical fractionation of the bulk composition  
187 due to the growth of the strongly zoned garnet porphyroblasts have been also considered. The bulk  
188 composition effectively in equilibrium during the growth of garnet rim has been therefore calculated by  
189 subtracting the garnet core and mantle compositions (i.e. the modal amount of garnet core + mantle was  
190 estimated from the micro-XRF maps as 3.5 vol%) to the whole rock composition (Table 1).

191

## 192 **4. Petrography and mineral chemistry**

193 Among the various lithologies observed in the study area, two metasediments (samples 14-4B and 14-6F/G)  
194 have been petrologically investigated in detail; they are both characterized by a relatively simple and very  
195 well preserved mineral assemblage, but differ for the grain size and the modal abundance of each phase  
196 (Table 1). Samples 14-6F/G derive from the same hand specimen (two different thin sections cut parallel  
197 and perpendicular to the main lineation); petrography and mineral chemistry refer to both thin sections,  
198 whereas the micro-XRF map and the thermodynamic modeling refer to sample 14-6F only.

199

### 200 **4.1 Sample 14-4B**

201 Sample 14-4B is a fine-grained lawsonite + glaucophane + garnet -bearing quartzitic-micaschist  
202 characterized by mm-thick quartz-rich layers alternating with mm-thick lawsonite + phengite-rich layers

203 (Fig. 4a). The main foliation, defined by the preferred orientation of phengite and glaucophane in both  
204 domains, is crosscut by late quartz-bearing and calcite ± albite -bearing veins (Fig. 3, and Fig. SM1).

205 Microstructural relationships between quartz (42 vol%), lawsonite (21 vol%), phengite (22 vol%),  
206 glaucophane (12 vol%) and garnet (3 vol%) suggest that these minerals all belong to the equilibrium  
207 assemblage (Fig. 7). Abundant titanite and minor pyrite occur as accessory minerals.

208 Lawsonite occurs as fine-grained idiomorphs (Fig. 4) with quartz ± titanite inclusions; in the quartz-rich layers,  
209 lawsonite is often crowded of quartz inclusions, locally assuming a skeletal habit. It is almost pure in  
210 composition, with a very low Fe content (0.00-0.30 a.p.f.u. on the basis of 8 oxygens).

211 The fine-grained phengite (Fig. 4b,c) shows a relatively large compositional spread in Si, Al<sub>tot</sub> and (Mg +  
212 Fe<sub>tot</sub>). Its Si content ranges between 3.53 and 3.81 a.p.f.u. (on the basis of 11 oxygens), with the most  
213 frequent values in the range 3.53-3.64 a.p.f.u (Fig. 6d). Most of the phengite compositions broadly lie along  
214 the celadonite-muscovite compositional joint, reflecting the dominant role of Tschermak's substitution;  
215 phengite with the lowest Si contents, however, plot slightly away from the celadonite- muscovite joint in  
216 both Si vs. Al<sub>tot</sub> and (Mg + Fe<sub>tot</sub>) vs. Si diagrams, thus suggesting the existence of very low Fe<sup>+3</sup> contents  
217 (Vidal and Parra, 2000).

218 Blue amphibole occurs as fine-grained idiomorphs associated to phengite and lawsonite (Fig. 4a,b), and it is  
219 slightly zoned, with a lighter blue core and a darker blue rim. Both cores and rims are ferroglaucophane  
220 according to the classification of Leake et al. (1997), but are characterized by slightly different Si (on the  
221 basis of 23 oxygens), XNa (XNa=Na/Na+Ca) and XFe<sup>+3</sup> (XFe<sup>+3</sup>=Fe<sup>+3</sup>/Fe<sub>tot</sub>) contents (core: Si = 7.62-7.74  
222 a.p.f.u., XNa=0.92-0.95, XFe<sup>+3</sup>=0.23-0.27; rim: Si = 7.91-7.97 a.p.f.u., XNa=0.98-1.00, XFe<sup>+3</sup>=0.10-0.21) (Fig.  
223 6e,f).

224 Garnet occurs as small slightly zoned idiomorphs (up to 0.3 mm in diameter) (Fig. 4a), particularly enriched in  
225 Mn (Fig. 6a). XSp<sub>s</sub> decreases and XAlm and XPrp increase from core to rim, whereas XGrs is almost  
226 homogeneous (core: Sps<sub>55-60</sub>Alm<sub>20-25</sub>Grs<sub>15-22</sub>Prp<sub>0-0.6</sub>; mantle: Sps<sub>50-54</sub>Alm<sub>25-28</sub>Grs<sub>16-23</sub>Prp<sub>0.4-0.9</sub>; rim: Sps<sub>44-47</sub>Alm<sub>30-</sub>  
227 <sub>34</sub>Grs<sub>18-23</sub>Prp<sub>0.6-1.3</sub>) (Fig. 6a).

228

#### 229 **4.2 Sample 14-6F/G**

230 Sample 14-6F/G is a lawsonite + glaucophane + phengite + garnet schist, dominated by glaucophane (44  
231 vol%) + lawsonite (22 vol%) + phengite (9 vol%) + garnet (4 vol%) layers alternating with discontinuous  
232 quartz (21 vol%) -rich domains. The main foliation, defined by the preferred orientation of glaucophane and  
233 minor phengite, is overgrown by large lawsonite and garnet porphyroblasts and it is intensely crenulated  
234 (Fig. 5a,b). Lawsonite and garnet porphyroblasts crystallization occurred prior to the crenulation event (Fig.  
235 7). Titanite occurs as accessory mineral aligned to the main foliation. Late quartz ± albite ± chlorite veins  
236 crosscut the main foliation (Fig. 5d, e).

237 The fine-grained blue amphibole nematoblasts in the matrix (Fig. 5a-c) are quite homogeneous in  
238 composition; they are glaucophane according to the classification of Leake et al. (1997) and have Si = 7.71-  
239 7.99 a.p.f.u., XNa=0.85-1.00 and XFe<sup>+3</sup>=0.14-0.24, with Si and XNa decreasing and XFe<sup>+3</sup> increasing toward  
240 the rim (Fig. 6e,f).

241 Lawsonite occurs as large porphyroblasts, up to few centimeter in size, overgrowing the main foliation (Fig.  
242 3, 5a-d and Fig. SM2). Lawsonite porphyroblasts are often boudinated; the boudinage still occurred in the  
243 lawsonite stability field because lawsonite + quartz + glaucophane are also found in the pressure shadows  
244 (Fig. 5c). The Fe content in lawsonite is very low (Fe = 0.03-0.05 a.p.f.u. on the basis of 8 oxygens).

245 Garnet porphyroblasts, up to 2-3 mm in diameter, overgrow the main foliation and are also included in  
246 lawsonite (Fig. 5). They are strongly zoned (Fig. 5e, 6a, 6b), with spessartine decreasing and almandine and  
247 pyrope increasing from core to rim (core: Sps<sub>50-55</sub>Alm<sub>16-21</sub>Grs<sub>26-28</sub>Prp<sub>1.1-1.4</sub>; mantle: Sps<sub>40-48</sub>Alm<sub>22-27</sub>Grs<sub>29-</sub>  
248 <sub>31</sub>Prp<sub>1.5-1.8</sub>; rim: Sps<sub>24-30</sub>Alm<sub>37-42</sub>Grs<sub>27-32</sub>Prp<sub>2.5-3.4</sub>) (Fig. 6a). Garnet porphyroblasts include glaucophane,

249 actinolite, quartz and chlorite in the core and mantle domains, and few omphacite ( $Jd_{16-33}Acm_{9-17}$ ) (Fig. 6c),  
250 phengite (Si = 3.80 a.p.f.u.) and quartz in the mantle and rim domains (Fig. 5e,5f, 6d).  
251 Phengite occurs as small flakes in equilibrium with glaucophane (Fig. 5, 7); it is locally zoned, with the  
252 highest Si content in the rim (core: Si=3.36-3.57 a.p.f.u.; rim: Si=3.61-3.84 a.p.f.u. on the basis of 11  
253 oxygens). The  $Fe^{+3}$  content in phengite is low since most of the phengite compositions lie along the  
254 celadonite-muscovite compositional joint (Fig. 6d).

255

## 256 **5. Phase equilibria and P-T evolution**

### 257 **5.1 P-T pseudosection in the MnNKCFMASH system**

258 The thermodynamic modeling approach was used to constrain the P-T evolution of the two blueschist  
259 samples. P-T pseudosections have been first calculated in the MnNKCFMASH model system (MnO-Na<sub>2</sub>O-  
260 K<sub>2</sub>O-CaO-FeO-MgO-Al<sub>2</sub>O<sub>3</sub>-SiO<sub>2</sub>-H<sub>2</sub>O), and two assumptions were made: (1) H<sub>2</sub>O was considered in excess; (2)  
261  $Fe^{+3}$  was not included in the calculation. The influence of these two important components on the stability  
262 of mineral assemblages will be discussed later. Concerning sample 14-6F, the fractionation effects on its  
263 bulk composition due to the growth of large garnet porphyroblasts have been considered, and two  
264 different pseudosections have been calculated: (i) a first pseudosection, calculated using the whole rock  
265 composition, has been used to model the growth of garnet core + mantle; (ii) a second pseudosection,  
266 calculated using the effective bulk composition derived by subtracting garnet cores and mantles to the  
267 whole rock composition (Table 1), has been used to model the growth of garnet rim. Fractionation effects  
268 on the bulk composition are negligible for sample 14-4B, because garnet is very small.

269

#### 270 *5.1.1 P-T evolution constrained for sample 14-4B*

271 The topology of the pseudosection calculated for sample 14-4B is very simple and dominated by three- and  
272 four-variant fields (Fig. 8a). The observed peak assemblage Grt + Gln + Lws + Phe is modelled by a relatively  
273 narrow five-variant field at  $P > 19$  kbar, which separates a chlorite-bearing field (at lower T) from an  
274 omphacite-bearing field (at higher T). At  $P < 19$  kbar, both chlorite and omphacite coexist in the three-  
275 variant Grt + Gln + Lws + Phe + Chl + Omp field.

276 The modeled garnet compositional isopleths (core:  $X_{Sps}=0.60$ ,  $X_{Alm}=0.24$ ,  $X_{Grs}=0.15$ ,  $X_{Prp}=0.006$ ; mantle:  $X_{Sps}=$   
277  $0.52$ ,  $X_{Alm}=0.28$ ,  $X_{Grs}=0.18$ ,  $X_{Prp}=0.009$ ; rim:  $X_{Sps}=0.44$ ,  $X_{Alm}=0.30$ ,  $X_{Grs}=0.23$ ,  $X_{Prp}=0.013$ ) constrain the growth  
278 of garnet core, mantle and rim at about 365 °C, 19.5 kbar (in the Grt + Gln + Lws + Phe + Chl field), 390°C,  
279 20.5 kbar (in the Grt + Gln + Lws + Phe field) and 420°C, 22 kbar (in the Grt + Gln + Lws + Phe + Omp field)  
280 (Fig. 8a and Fig. SM3). The modeled modal amounts of chlorite and omphacite in equilibrium with garnet  
281 core and rim, respectively, are lower than 0.5 vol%. The modeled phengite compositional isopleths (Si =  
282 3.80-3.82 a.p.f.u.) constrain the growth of phengite at P-T conditions compatible with the growth of garnet  
283 core and mantle.

284 The resulting prograde P-T evolution of sample 14-4B is therefore characterized by an increase in both P  
285 and T, up to peak conditions of about 420°C, 22 kbar (Fig. 8a). The modeled isomodes of the main mineral  
286 phases are consistent with the prograde growth (i.e. increase in its modal amount) of garnet along this P-T  
287 path, but predict the (slight) consumption of lawsonite (Fig. 8b; the P-T path crosses the Lws-isomodes  
288 downward), opposite to microstructural observations which suggest that garnet and lawsonite grew almost  
289 simultaneously (Fig. 7). This apparent discrepancy between the results of the thermodynamic modeling and  
290 the observed microstructure will be discussed in the following. The modeled H<sub>2</sub>O isomodes show that  
291 during the inferred prograde evolution, a moderate de-hydration occurred, thus implying that mineral  
292 assemblages were H<sub>2</sub>O saturated (Guiraud et al., 2001).

293

### 294 5.1.2 P-T evolution constrained for sample 14-6F

295 The topologies of the two pseudosections calculated for sample 14-6F using the whole rock composition  
296 and the fractionated bulk composition are simple and dominated by three- and four-variant fields. Because  
297 the two pseudosections are quite similar (the main difference is the shift of the Grt-bearing fields toward  
298 higher temperatures in the fractionated pseudosection), they have been condensed in the same figure (Fig.  
299 9a). Two large three-variant fields, separated by a narrow di-variant field, dominate the two  
300 pseudosections: at higher P (and lower T) is stable the Chl + Grt + Act + Gln + Lws + Phe assemblage,  
301 whereas at lower P (and higher T) is stable the Chl + Grt + Gln + Lws + Omp + Phe assemblage.

302 The modeled garnet compositional isopleths from the unfractionated pseudosection (core:  $X_{\text{Sps}}=0.55$ ,  
303  $X_{\text{Alm}}=0.18$ ,  $X_{\text{Grs}}=0.27$ ,  $X_{\text{Prp}}=0.011$ ; mantle:  $X_{\text{Sps}}=0.40$ ,  $X_{\text{Alm}}=0.27$ ,  $X_{\text{Grs}}=0.30$ ,  $X_{\text{Prp}}=0.018$ ) constrain the growth of  
304 garnet core and mantle at about 395 °C, 18.5 kbar (in the Chl + Grt + Act + Gln + Lws + Phe field) and 435°C,  
305 19.5 kbar (in the Chl + Grt + Gln + Lws + Omp + Phe field) (Fig. 9a and Fig. SM4). The transition from the Act-  
306 bearing (Omp-absent) field to the Omp-bearing (Act-absent) field is consistent with the occurrence of  
307 actinolite inclusions within garnet core, and omphacite inclusions within garnet mantle. The modeled  
308 phengite compositional isopleths (Si = 3.81-3.83 a.p.f.u.) constrain the growth of phengite at P-T conditions  
309 slightly lower than the growth of garnet core.

310 The modeled garnet compositional isopleths from the fractionated pseudosection (rim:  $X_{\text{Sps}}=0.24$ ,  
311  $X_{\text{Alm}}=0.42$ ,  $X_{\text{Grs}}=0.31$ ,  $X_{\text{Prp}}=0.034$ ) constrain the growth of garnet rim at about 470 °C, 20 kbar (in the Chl +  
312 Grt + Gln + Omp + Lws + Phe field) (Fig. 9a). The modeled modal amount of chlorite in equilibrium with  
313 garnet rim is lower than 1 vol%.

314 Peak P-T conditions for sample 14-6F are therefore constrained at about 470 °C, 20 kbar. Overall, the  
315 prograde P-T evolution of sample 14-6F is similar in shape to that predicted for sample 14-4B but at lower P  
316 and slightly higher T (i.e.  $\Delta T = + 50$  °C,  $\Delta P = -2$  kbar). Similarly to sample 14-4B, the modeled isomodes do  
317 not predict the growth (i.e. increase in modal amount) of lawsonite along this P-T path (Fig. 9b), opposite to  
318 microstructural observation which clearly show that lawsonite grew simultaneously (or even later) to  
319 garnet (Fig. 7).

320

### 321 5.2 The influence of $\text{Fe}^{+3}$

322 Although low, the  $\text{Fe}^{+3}$  content in glaucophane from both the samples is not negligible, suggesting that the  
323 metasediment bulk compositions were slightly oxidized. In order to test the influence of  $\text{Fe}^{+3}$  on the  
324 stability of the equilibrium assemblages and on the peak P-T conditions, two P- $\text{XFe}_2\text{O}_3$  and T- $\text{XFe}_2\text{O}_3$   
325 pseudosections were calculated at 420°C, 22 kbar (sample 14-4B; Fig. 10a,b), and 470°C, 20 kbar (sample  
326 14-6F; Fig. 10c,d), respectively, i.e. at the peak P-T conditions estimated for the two samples in the  $\text{Fe}^{+3}$ -free  
327 MnNKCFMASH system. A  $\text{XFe}_2\text{O}_3$  range of 0-0.5 was considered, with  $\text{XFe}_2\text{O}_3 = \text{Fe}_2\text{O}_3/\text{FeO}_{\text{tot}}$  (i.e.  $\text{XFe}_2\text{O}_3 = 0$   
328 means that all Fe is bivalent;  $\text{XFe}_2\text{O}_3 = 0.5$  means that FeO and  $\text{Fe}_2\text{O}_3$  are present in equal amounts).

329 The P- $\text{XFe}_2\text{O}_3$  and T- $\text{XFe}_2\text{O}_3$  pseudosections modeled for sample 14-4B and contoured for the garnet rim  
330 compositional isopleths, show that peak-P conditions decrease of about 2-3 kbar with increasing  $\text{XFe}_2\text{O}_3$ ,  
331 whereas peak-T conditions do not significantly change at variable  $\text{XFe}_2\text{O}_3$  values. The  $\text{XFe}_2\text{O}_3$  is constrained  
332 to a maximum of 0.20, above which the modeled peak assemblage (Grt + Gln + Lws + Phe + minor Omp) is  
333 no longer stable (Fig. 10a,b).

334 The same effects are also observed for sample 14-6F, but in this case the decrease of peak-P conditions is  
335 less pronounced (ca. 1 kbar). The stability field of the peak assemblage (Grt + Gln + Omp + Lws + Phe +  
336 minor Chl) constrains the maximum  $\text{XFe}_2\text{O}_3$  value to 0.4, but for  $\text{XFe}_2\text{O}_3 > 0.15$  the modeled garnet  
337 compositional isopleths diverge, therefore constraining  $\text{XFe}_2\text{O}_3$  to values in the range 0-0.15 (Fig. 10c,d).



338 The P-T paths of the two studied samples calculated for  $X_{\text{Fe}_2\text{O}_3}=0.10$  mostly overlap, thus suggesting that  
339 the prograde P-T evolution of the SSOM blueschists was characterized by an increase in P and T from ca.  
340 370 °C, 17 kbar to peak conditions of ca. 470°C, 19 kbar.

341

## 342 **6. Discussion**

### 343 **6.1 $\text{H}_2\text{O}$ -saturated vs. $\text{H}_2\text{O}$ under-saturated conditions**

344 The results obtained so far are based on the assumption that  $\text{H}_2\text{O}$  was in excess during the whole  
345 metamorphic evolution: this is a common assumption in the modeling of lawsonite-bearing blueschist and  
346 eclogites (e.g. Davis and Whitney, 2006, 2008; Clarke et al., 2006; Groppo and Castelli, 2010; Endo et al.,  
347 2012; Wei and Clarke, 2011; Vitale Brovarone et al., 2011; Ao and Bhowmik, 2014; Tian and Wei, 2014;  
348 Bhowmik and Ao, 2015). In many cases  $\text{H}_2\text{O}$  is considered in excess because lawsonite-bearing assemblages  
349 demand that high water amounts are available in the system. Opposite to this common assumption, it has  
350 also been demonstrated that lawsonite can grow during subduction (at increasing P and T) at  $\text{H}_2\text{O}$ -  
351 undersaturated conditions (e.g. Balleuvre et al., 2003; Lopez-Carmona et al., 2013).  $\text{H}_2\text{O}$ -undersaturated  
352 conditions would significantly influence phase equilibria and hence P-T estimates; therefore, the possibility  
353 that prograde metamorphism could have occurred under  $\text{H}_2\text{O}$ -undersaturated conditions should be  
354 carefully evaluated.

355 This issue was explored by calculating two P/T- $X(\text{H}_2\text{O})$  pseudosections for sample 14-4B (Fig. 11); similar  
356 results are obtained for sample 14-6F (see Fig. 12a). These pseudosections report the  $\text{H}_2\text{O}$  content (in wt%)  
357 on the horizontal axis and a P/T gradient on the vertical axis. Two P/T gradients have been considered: the  
358 first one (gradient A: Fig. 11a) is coincident with the P-T path constrained using the P-T pseudosection  
359 calculated with  $\text{H}_2\text{O}$  in excess, whereas the second one (gradient B: Fig. 11b) is steeper and similar to the  
360 early prograde P-T evolution of Eastern Himalayan blueschists reported in the literature (Ao and Bhowmik.,  
361 2014). The two pseudosections are contoured for garnet core and rim compositions. The intersection  
362 between garnet compositional isopleths should provide information about: (i) whether the growth of  
363 garnet with the measured composition could have occurred along the previously discussed P/T gradient A  
364 but at  $\text{H}_2\text{O}$ -undersaturated conditions, and (ii) whether the alternative (steeper) P/T gradient B would be  
365 compatible with the growth of garnet with the measured composition under  $\text{H}_2\text{O}$ -undersaturated  
366 conditions.

367 The white dotted lines in the calculated P/T- $X(\text{H}_2\text{O})$  pseudosections represent the  $\text{H}_2\text{O}$ -saturation surface  
368 and divide the pseudosections in a  $\text{H}_2\text{O}$ -saturated part on the right and in a  $\text{H}_2\text{O}$ -undersaturated part on the  
369 left. A  $\text{H}_2\text{O}$  amount of 3-4 wt% (depending on T and P) is required to reach  $\text{H}_2\text{O}$ -saturated conditions in  
370 sample 14-4B. Garnet compositional isopleths show that: (i) the steeper P/T gradient B (Fig. 11b) is not  
371 compatible with the observed garnet compositions because the modeled compositional isopleths of garnet  
372 core do not overlap; (ii) concerning the P/T gradient A, the intersection of garnet compositional isopleths  
373 on the  $\text{H}_2\text{O}$ -saturation surface confirms that the growth of garnet with the measured composition occurred  
374 at  $\text{H}_2\text{O}$ -saturated conditions (Fig. 11a, 12a), thus suggesting that the assumption of  $\text{H}_2\text{O}$  in excess for the  
375 modeling of garnet growth was correct.

376

### 377 **6.2 When and how did lawsonite grow**

378 The P/T- $X(\text{H}_2\text{O})$  pseudosections calculated at  $\text{H}_2\text{O}$  saturated conditions for both samples 14-4B (Fig. 8) and  
379 14-6F (Fig. 9) fail in modeling the contemporaneous growth of lawsonite and garnet; in fact, the inferred  
380 prograde P-T path crosses the garnet isomodes upward (Fig. 8c, 9c), but the lawsonite isomodes are  
381 crossed downward (Fig. 8b, 9b), thus suggesting that lawsonite was (slightly) consumed when garnet was  
382 growing (i.e. lawsonite modal amount was slightly decreasing while garnet modal amount was increasing).

383 Two different hypothesis can be proposed to explain the discrepancy between the observed  
384 microstructures and the prediction of thermodynamic modeling: (i) the first hypothesis is still based on an  
385 equilibrium model for prograde metamorphism, which is the classical paradigm that is the basis of  
386 isochemical phase diagrams; (ii) the second hypothesis explores the possibility that the prograde  
387 appearance of lawsonite was controlled by nonequilibrium processes rather than by equilibrium ones (i.e.  
388 kinetics factors prevailing over equilibrium thermodynamics).

389

#### 390 *6.2.1 The equilibrium approach*

391 Following an approach based on the principles of equilibrium thermodynamics, the P/T-X(H<sub>2</sub>O)  
392 pseudosection calculated for sample 14-6F (Fig. 12a), contoured for lawsonite and garnet modal amounts  
393 (Fig. 12b, 12c) is useful to explain the inconsistency between the observed and predicted sequence of  
394 porphyroblasts growth (i.e. Lws contemporaneous with Grt vs. Lws earlier than Grt) (see also Fig. SM5 for  
395 sample 14-4B). Fig. 12b shows that H<sub>2</sub>O addition is required to form lawsonite (i.e. to increase its modal  
396 amount). The observed microstructures suggest that lawsonite growth was contemporaneous to garnet  
397 growth (Fig. 7), thus implying that H<sub>2</sub>O was introduced in the system at the relatively high pressure of ca.  
398 17-18 kbar (large white arrow in Fig. 12b). Once reached H<sub>2</sub>O-saturated conditions, garnet (with the  
399 measured composition of Grt core) started to form; the simultaneous growth of high modal amounts of  
400 lawsonite, however, subtracted H<sub>2</sub>O to the system (“-H<sub>2</sub>O” arrows in Fig. 12b), that eventually became  
401 again H<sub>2</sub>O-undersaturated. A protracted H<sub>2</sub>O influx at high pressure (“+H<sub>2</sub>O” arrows in Fig. 12b) is therefore  
402 required in order to allow the contemporaneous growth of garnet (which requires H<sub>2</sub>O-saturated  
403 conditions) and lawsonite (whose growth subtracts H<sub>2</sub>O to the system).

404 Our model thus suggests that the system might have been H<sub>2</sub>O-undersaturated during the early prograde  
405 subduction (i.e. prior to the appearance of garnet). According to the modeling, at H<sub>2</sub>O-undersaturated  
406 conditions, the Ca-rich precursor of lawsonite should have been epidote: the small epidote inclusions  
407 observed in garnet porphyroblasts (sample 14-6F: Fig. 5f) would support this assumption. This hypothesis  
408 confirms what has been already predicted by previous studies, i.e. the H<sub>2</sub>O-rich character of lawsonite-  
409 bearing assemblages requires the addition of H<sub>2</sub>O at elevated pressure to allow them to form (Clarke et al.,  
410 2006; Tsujimori and Ernst, 2014). Significant fluid release is predicted at these P-T conditions (e.g. Ulmer  
411 and Trommsdorff, 1995; Scambelluri et al., 2004; Poli and Schmidt, 1995; Poli et al., 2009) through  
412 metamorphic devolatilization reactions occurring in the subducting slab (Bebout, 1991, 1995; Jarrad, 2003).  
413 Our results suggest that fluids released at P > 17-18 kbar by the de-hydrating subducting slab can be largely  
414 re-incorporated in lawsonite, and confirm that the pervasive growth of lawsonite represents an efficient  
415 mechanism for fixing water in the high pressure accretionary prism, thereby delaying its ascent toward the  
416 surface (Ballèvre et al., 2003; Vitale Brovarone and Beyssac, 2014).

417

#### 418 *6.2.2 The nonequilibrium approach*

419 Alternatively to what discussed in the previous point, the inconsistency between the observed  
420 microstructures and the equilibrium phase relations predicted by the pseudosections could suggest that  
421 nonequilibrium processes controlled the prograde appearance of lawsonite and garnet. Transient  
422 nonequilibrium states can be common during prograde metamorphism (e.g. Ague & Carlson, 2013),  
423 especially at low temperatures such those inferred for the early prograde evolution of the studied  
424 blueschists. Previous works addressed the question of the interplay between the approach to equilibrium  
425 on one hand, and reaction kinetics on the other hand (see Ague & Carlson, 2013 for a review). Crucial to the  
426 discussion is the concept of reaction affinity, which is an energetic expression of the easiness of a reaction  
427 to overstep the kinetic barriers to nucleation and growth (e.g. Waters & Lovegrove, 2002; Pattison et al.,  
428 2011; Ketcham & Carlson, 2012). It has been demonstrated that mineral reactions which release large

429 quantities of H<sub>2</sub>O have higher reaction affinity per unit of temperature/pressure overstep than those which  
430 release little or no H<sub>2</sub>O. The former are expected to be overstepped in temperature and/or pressure less  
431 than the latter (see Pattison et al., 2011 for further details). Reactions with lower reaction affinity may be  
432 strongly influenced by kinetic factors, or may not occur at all.

433 Some authors considered nucleation as the main rate-limiting process in metamorphic reactions (e.g.  
434 Waters & Lovegrove, 2002; Gaidies et al., 2011; Pattison et al., 2011). They demonstrated that low reaction  
435 affinity (and consequently high overstepping) of a prograde metamorphic reaction may cause the delayed  
436 nucleation (and growth) of porphyroblastic phases. Microstructurally, this becomes evident when the  
437 observed sequence of porphyroblasts growth does not coincide with the sequence predicted by  
438 thermodynamic modelling (e.g. Waters & Lovegrove, 2002). Other authors argued that intergranular  
439 diffusion is the main kinetic component controlling the nucleation and growth of porphyroblastic phases  
440 (e.g. Carlson, 1989, 2002; Hirsch et al., 2000; Ketcham & Carlson, 2012). In this case, delayed porphyroblasts  
441 growth would be related to the sluggishness of intergranular diffusion. More in detail, growing  
442 porphyroblasts extract nutrients from the immediate surroundings, suppressing the nucleation of new  
443 crystals in diffusionally depleted zones surrounding pre-existing crystals.

444 A quantitative treatment of these concepts is well beyond the aim of this paper; nevertheless, it is worth  
445 nothing that the modelled pseudosection for sample 14-6F predicts that lawsonite is mainly produced at  
446 low P-T conditions (i.e. at P < 5 kbar, and T < 300°C; Fig. SM6) through the epidote or prehnite (depending  
447 on T) breakdown, much earlier than the onset of garnet growth. Both the epidote- and prehnite-  
448 consuming (lawsonite-producing) reactions are hydration reactions, i.e. they consume H<sub>2</sub>O. Qualitatively,  
449 it is therefore to be expected that reaction affinity of these reactions is very low and that they might be  
450 significantly overstepped in temperature and pressure. The discrepancy between the observed and  
451 predicted sequence of porphyroblasts growth can be therefore explained by a delayed growth of lawsonite  
452 porphyroblasts, possibly due to: (i) low reaction affinity of the Lws-producing reaction (either Ep- or Prh-  
453 consuming), and/or (ii) difficulty of nucleation of lawsonite.

454 Both the equilibrium- and nonequilibrium- hypothesis are compatible with microstructural observations  
455 (e.g. the rare occurrence of small epidote inclusions within garnet) and they are complementary rather  
456 than mutually exclusive.

### 457 458 **6.3 Interpretation of the P-T evolution and geodynamic implications**

459 Prior to this study, P-T estimates based on conventional thermobarometry suggested peak P-T conditions of  
460 350-420°C, 9-11 kbar for the SSOM blueschists (Honegger et al., 1989). The results of our petrological  
461 modeling point to peak P-T conditions significantly higher than those previously estimated, i.e. ca. 470°C,  
462 19 kbar (Fig. 13), thus suggesting that the careful re-examination (by means of modern petrological  
463 approaches) of previous P-T estimates obtained using conventional thermobarometry can provide new  
464 insights on the subduction history of the Neo-Tethyan ocean. The obtained results suggest that the SSOM  
465 blueschists experienced a cold subduction history along a very low to low thermal gradient (“early”  
466 prograde: ca. 5-6°C/km; “late” prograde: ca. 7-8°C/km; Fig. 13a). Furthermore, in order to preserve  
467 lawsonite in the studied lithologies, exhumation must have been coupled with significant cooling (i.e.  
468 without crossing the lawsonite-out boundary; Zack et al., 2004). The resulting P-T path is therefore  
469 characterized by a clockwise hairpin loop along low thermal gradients (< 8-9 °C/km) (Fig. 13a).

470 This P-T evolution is consistent with a cold subduction zone system in an intra-oceanic subduction setting,  
471 as also suggested by Ao and Bhowmik (2014) for blueschists from the far eastern Himalaya. Moreover, the  
472 observed lithological associations (i.e. mainly volcanoclastic rocks and minor sediments), the estimated  
473 peak P-T conditions (very close to the eclogite stability field but still inside the lawsonite blueschist -facies)  
474 and the clockwise hairpin P-T trajectory, are all consistent with the interpretation that the SSOM represents

475 a relic of an oceanic paleo-accretionary prism, related to the northward subduction of the northern Neo-  
476 Tethyan ocean beneath the Ladakh Asian margin (Robertson, 2000; Mahéo et al., 2006; Guillot et al., 2008).  
477 Interestingly, the estimated peak P-T conditions of ca. 470°C, 19 kbar roughly coincide with the maximum  
478 P-T estimates predicted by thermo-mechanical models for the metasediments exhumed in the accretionary  
479 wedge (Yamato et al. 2007) (Fig. 13a), and with the maximum P-T conditions registered by natural  
480 occurrences of blueschist accretionary complexes worldwide (Fig. 13b) (e.g. the Schistes Lustres Complex of  
481 the Western Alps and Alpine Corsica, Turkey, Zagros, Oman, New Caledonia, Franciscan Complex: e.g.  
482 Banno et al., 2000; Agard et al., 2001a,b; Warren et al., 2005; Agard et al., 2006; Page et al., 2006; Tsujimori et  
483 al., 2006; Warren and Waters, 2006; Ernst and McLaughlin, 2012; Plunder et al., 2012, 2015; Agard and  
484 Vitale Brovarone, 2013; Ukar and Cloos, 2014; Vitale Brovarone et al., 2014).

485 Most of the studies focused on subduction-related HP-LT terranes from different localities point to a  
486 continuous increase of peak-T and associated P in adjacent tectonometamorphic units (Fig. 13b). A  
487 continuous metamorphic gradient is thus recorded in most of the blueschist-facies terranes worldwide, up  
488 to maximum P-T conditions of ca. 470°C, 18-19 kbar (e.g. Oman: Yamato et al., 2007; Corsica: Vitale  
489 Brovarone et al., 2014; Schistes Lustres of the Western Alps: Plunder et al., 2012; New Caledonia: Vitale  
490 Brovarone & Agard, 2013; Turkey: Plunder et al., 2015). This metamorphic zonation might reflect the  
491 repeated accretion of the ocean-floor sediments subducted at different depths and offscraped at the base  
492 of the accretionary prism (e.g. Agard et al., 2009 and references therein).

493 A similar metamorphic zonation from greenschist to pumpellyite-diopside and up to lawsonite-blueschist -  
494 facies conditions has been recently reported by Ao & Bhowmik (2014) for the Nagaland Ophiolite Complex  
495 of far-eastern Himalaya, whose geological setting is very similar to that of the SSOM (i.e. it is mainly  
496 dominated by metavolcanoclastic rocks, with minor intercalations of metasediments). Although a detailed  
497 discussion of the SSOM metamorphic units adjacent to the blueschist one is beyond the aim of this paper, it  
498 is worth mentioning that preliminary data suggest that a similar metamorphic zonation might characterize  
499 also the western portion of the ITS zone. Chlorite + epidote + green/blue-green amphibole -bearing  
500 metavolcanoclastic rocks, and prehnite-pumpellyite -bearing metagabbros occur in the thin metamorphic  
501 slices associated to the blueschist unit in the SSOM. Further petrological investigations could eventually  
502 confirm the existence of a continuous metamorphic gradient in the SSOM.

503

504

## 505 **Acknowledgements**

506 This study is part of a Cooperation Agreement between the University of Torino, Dept. of Earth Sciences  
507 (Torino, Italy) and the Wadia Institute of Himalayan Geology (Dehradun, India). Fieldwork was supported by  
508 University of Torino—Call 1—Junior PI Grant (TO\_Call1\_2012\_0068); laboratory work was supported by the  
509 Italian Ministry of University and Research (PRIN 2011 - 2010PMKZX7) and Ricerca Locale (ex-60% - 2014)  
510 funds of the University of Torino. We thank A. Vitale Brovarone for useful discussions on lawsonite-bearing  
511 rocks. Constructive reviews from S. Guillot and an anonymous reviewer improved the final manuscript.

512 **References**

- 513 Abers, G.A., Nakajima, J., van Keken, P.E., Kita, S., Hacker, B.R., 2013. Thermal-petrological controls on the  
514 location of earthquakes within subducting plates. *Earth and Planetary Science Letters* 369–370, 178–187.
- 515 Acharyya, S.K., 1986. Tectono-stratigraphic history of Naga Hills Ophiolites, in: Ghosh, D.B. (ed.), *Geology of*  
516 *the Nagaland Ophiolite*. Geological Survey of India Memoirs 119, 94-103.
- 517 Agard, P., Monié, P., Gerber, W., Omrani, J., Molinaro, M., Meyer, B., Labrousse, L., Vrielynck, B., Jolivet, L.,  
518 Yamato, P., 2006. Transient, syn-obduction exhumation of Zagros blueschists inferred from P–T-  
519 deformation-time and kinematic constraints: implications for Neotethyan wedge dynamics. *Journal of*  
520 *Geophysical Research* 111, B11401.
- 521 Agard, P., Jolivet, L., Goffé, B., 2001a. Tectonometamorphic evolution of the Schistes Lustrés complex:  
522 implications for the exhumation of HP and UHP rocks in the Western Alps. *Bulletin de la Société*  
523 *Geologique de France* 172, 617-636.
- 524 Agard, P., Vidal, O., Goffé, B., 2001b. Interlayer and Si content of phengite in carpholite-bearing  
525 metapelites. *Journal of Metamorphic Geology* 19, 479-495.
- 526 Agard, P., Vitale-Brovarone, A., 2013. Thermal regime of continental subduction: the record from exhumed  
527 HP-LT terranes (New Caledonia, Oman, Corsica). *Tectonophysics* 601, 206-215.
- 528 Agard, P., Yamato, P., Jolivet, L., Burov, J.E., 2009. Exhumation of oceanic blueschists and eclogites in  
529 subduction zones: timing and mechanisms. *Earth Science Reviews* 92, 53-79.
- 530 Ague, J.J., Carloson, W.D., 2013. Metamorphism as garnet sees it: the kinetics of nucleation and growth,  
531 equilibration and diffusional relaxation. *Elements* 9, 439-445.
- 532 Ahmad, T., Islam, R., Khanna, P., Thakur, V.C., 1996. Geochemistry, petrogenesis and tectonic significance  
533 of the basic volcanic units of the Zildat ophiolite mélange, Indus suture zone, eastern Ladakh (India).  
534 *Geodinamica Acta* 9, 222-233.
- 535 Ao, A., Bhowmik, S.K., 2014. Cold subduction of the Neotethys: the metamorphic record from finely  
536 banded lawsonite and epidote blueschists and associated metabasalts of the Nagaland Ophiolite  
537 Complex, India. *Journal of Metamorphic Geology* 32, 829-860.
- 538 Ballèvre, M., Pitra, P., Bohn, M., 2003. Lawsonite growth in the epidote blueschists from the Ile de Groix  
539 (Armorican Massif, France): a potential geobarometer. *Journal of Metamorphic Geology* 21, 723-735.
- 540 Banno, S., Shibakusa, H., Enami, M., Wang, C.-L., Ernst, W.G., 2000. Chemical fine structure of Franciscan  
541 jadeitic pyroxene from Ward Creek, Cazadero area, California. *American Mineralogist* 85, 1795-1798.
- 542 Bebout, G.E., 1991. Field-based evidence for devolatilization in subduction zones: implications for arc  
543 magmatism. *Science* 251, 413–416.
- 544 Bebout, G.E., 1995. The impact of subduction-zone metamorphism on mantle-ocean chemical cycling.  
545 *Chemical Geology* 126, 191-218.
- 546 Bebout, G.E., 2007. Metamorphic chemical geodynamics of subduction zones. *Earth and Planetary Science*  
547 *Letters* 260, 373-393.
- 548 Bhowmik, S., Ao, A., 2015. Subduction initiation in the Neo-Tethys: constraints from counterclockwise P-T  
549 paths in amphibolite rocks of the Nagaland Ophiolite Complex, India. *Journal of Metamorphic Geology*,  
550 doi: 10.1111/jmg.12169
- 551 Cannat, M., Mascle, G., 1990. Réunion extraordinaire de la société géologique de France en Himalaya du  
552 Ladakh. *Bulletin de la Société Géologique de France* 4, 553-582.
- 553 Cao, Y., Jung, H., Song, S., 2013. Petro-fabrics and seismic properties of blueschist and eclogite in the North  
554 Qilian suture zone, NW China. Implications for the low-velocity upper layer in subducting slab, trench-  
555 parallel seismic anisotropy and eclogite detectability in the subduction zone. *Journal of Geophysical*  
556 *Research* 118, 3037–3058.

557 Carlson, W.D., 1989. The significance of intergranular diffusion to the mechanisms and kinetics of  
558 porphyroblast crystallization. *Contribution to Mineralogy and Petrology* 103, 1-24.

559 Carlson, W.D., 2002. Scales of disequilibrium and rates of equilibration during metamorphism. *American*  
560 *Mineralogist* 87, 185-204.

561 Chakungal, J., Dostal, J., Grujic, D., Duchêne, S., Ghalley, S.K., 2010. Provenance of the Greater Himalayan  
562 Sequence: Evidence from mafic eclogite-granulites and amphibolites in NW Bhutan. *Tectonophysics* 480,  
563 198-212.

564 Chantel, J., Mookherjee, M., Frost, D.J., 2012. The elasticity of lawsonite at high pressure and the origin of  
565 low velocity layers in subduction zones. *Earth and Planetary Science Letters* 349–350, 116-125.

566 Chatterjee, N., Ghose, N.C., 2010. Metamorphic evolution of the Naga Hills eclogite and blueschist,  
567 Northeast India: implications for early subduction of the Indian plate under the Burma microplate.  
568 *Journal of Metamorphic Geology* 28, 209-225.

569 Clarke, G.L., Powell, R., Fitzherbert, J.A., 2006. The lawsonite paradox: a comparison of field evidence and  
570 mineral equilibria modeling. *Journal of Metamorphic Geology* 24, 716-726.

571 Connolly, J.A.D., 1990. Multivariable phase diagrams: an algorithm based on generalized thermodynamics.  
572 *American Journal of Science* 290, 666-718.

573 Connolly, J.A.D., 2009. The geodynamic equation of state: what and how. *Geochemistry Geophysics*  
574 *Geosystems* 10, Q10014.

575 Cossio, R., Borghi, A., Ruffini, R., 2002. Quantitative modal determination of geological samples based on X-  
576 ray multielemental map acquisition. *Microscopy and Microanalysis* 8, 139-149.

577 Davis, P.B., 2011. Petrotectonics of lawsonite eclogite exhumation: Insights from the Sivrihisar massif,  
578 Turkey. *Tectonics* 30, TC1006.

579 Davis, P.B., Whitney, D.L., 2006. Petrogenesis of lawsonite and epidote eclogite and blueschist, Sivrihisar,  
580 Turkey. *Journal of Metamorphic Geology* 24, 823-849.

581 Davis, P.B., Whitney, D.L., 2008. Petrogenesis and structural petrology of high-pressure metabasalt pods,  
582 Sivrihisar, Turkey. *Contributions to Mineralogy and Petrology* 156, 217-241.

583 De Sigoyer, J., Chavagnac, V., Blichert-Toft, J., Villa, I.M., Luais, B., Guillot, S., Cosca, M., Mascle, G., 2000.  
584 Dating the Indian continental subduction and collisional thickening in the northwest Himalaya:  
585 multichronology of the Tso Moriri eclogites. *Geology* 28, 487-490.

586 De Sigoyer, J., Guillot, S., Dick, P., 2004. Exhumation Processes of the high pressure low-temperature Tso  
587 Moriri dome in a convergent context (eastern-Ladakh, NW-Himalaya). *Tectonics* 23, TC3003.

588 Diener, J.F.A., Powell, R., 2012. Revised activity-composition models for clinopyroxene and amphibole.  
589 *Journal of Metamorphic Geology* 30, 131–142.

590 Diener, J.F.A., Powell, R., White, R.W., Holland, T.J.B., 2007. A new thermodynamic model for clino- and  
591 orthoamphiboles in the system Na<sub>2</sub>O-CaO-FeO-MgO-Al<sub>2</sub>O<sub>3</sub>-SiO<sub>2</sub>-H<sub>2</sub>O-O. *Journal of Metamorphic Geology*  
592 25, 631-656.

593 Endo, S., Wallis, S.R., Tsuboi, M., Torres de Leon, R., Solari, A., 2012. Metamorphic evolution of lawsonite  
594 eclogites from the southern Motagua fault zone, Guatemala: insights from phase equilibria and Raman  
595 spectroscopy. *Journal of metamorphic geology* 30, 143-164.

596 Ernst, W.G., 1988. Tectonic history of subduction zones inferred from retrograde blueschist P–T paths.  
597 *Geology* 16, 1081-1084

598 Ernst, W.G., McLaughlin, R.J., 2012. Mineral parageneses, regional architecture, and tectonic evolution of  
599 Franciscan metagraywackes, Cape Mendocino-Garberville-Covelo 30' × 60' quadrangles, northwest  
600 California. *Tectonics* 31, TC1001.

601 Fitzherbert, J.A., Clarke, G.L., Marmo, B., Powell, R., 2004. The Origin and P–T evolution of peridotites and  
602 serpentinites of NE New Caledonia: prograde interaction between continental margin and the mantle  
603 wedge. *Journal of Metamorphic Geology* 22, 327-344.

604 Fitzherbert, J.A., Clarke, G.L., Powell, R., 2005. Preferential retrogression of high-P metasediments and the  
605 preservation of blueschist to eclogite facies metabasite during exhumation, Diahot terrane, NE New  
606 Caledonia. *Lithos* 83, 67-96.

607 Fitzherbert, J.A., Clarke, G.L., Powell, R., Powell, R., 2003. Lawsonite-omphacite-bearing metabasites of the  
608 Pam Peninsula, NE New Caledonia: evidence for disrupted blueschist- to eclogite-facies conditions.  
609 *Journal of Petrology* 44, 1805-1831.

610 Frank, W., Gansser, A., Trommsdorff, V., 1977. Geological observations in the Ladakh area (Himalayas): a  
611 preliminary report. *Schweizerische Mineralogische und Petrographische Mitteilungen* 57, 89-113.

612 Gaidies, F., Pattison, D.R.M., de Capitani, C., 2011. Toward a quantitative model of metamorphic nucleation  
613 and growth. *Contribution to Mineralogy and Petrology* 162, 975-993.

614 Ghose, N.C., Singh, R.N., 1980. Occurrence of blueschist facies in the ophiolite belt of Naga Hills, east of  
615 Kiphire, N.E., India. *Geologische Rundschau* 69, 41-43.

616 Green, E.C.R., Holland, T.J.B., Powell, R., 2007. An order-disorder model for omphacitic pyroxenes in the  
617 system jadeite-diopside-hedenbergite-acmite, with applications to eclogite rocks. *American Mineralogist*  
618 92, 1181-1189.

619 Groppo, C., Castelli, D., 2010. Prograde P–T evolution of a lawsonite eclogite from the Monviso meta-  
620 ophiolite (Western Alps): dehydration and redox reactions during subduction of oceanic FeTi-oxide  
621 gabbro. *Journal of Petrology* 51, 2489-2514.

622 Groppo, C., Lombardo, B., Rolfo, F., Pertusati, P., 2007. Clockwise exhumation path of granulitized eclogites  
623 from the Ama Drime range (Eastern Himalayas). *Journal of Metamorphic Geology* 25, 51-75.

624 Grujic, D., Warren, C., Wooden, J.L., 2011. Rapid synconvergent exhumation of Miocene-aged lower  
625 orogenic crust in the eastern Himalaya. *Lithosphere* 3, 346-366.

626 Guillot, S., Cosca, M., Allemand, P., Le Fort, P., 1999. Contrasting metamorphic and geochronologic  
627 evolution along the Himalayan belt, in: Macfarlane, A., Sorkhabi, R.B., Quade, J. (Eds.), *Himalaya and  
628 Tibet: Mountain Roots to Mountain Tops*. Geological Society of America, Boulder, Colorado. Special  
629 Paper, pp. 330.

630 Guillot, S., de Sigoyer, J., Lardeaux, J.M., Mascle, G., 1997. Eclogitic metasediments from the Tso Morari  
631 area (Ladakh, Himalaya): evidence for continental subduction during India–Asia convergence.  
632 *Contribution to Mineralogy and Petrology* 128, 197-212.

633 Guillot, S., Mahéo, G., de Sigoyer, J., Hattori, K.H., Pecher, A., 2008. Tethyan and Indian subduction viewed  
634 from the Himalayan high- to ultrahigh-pressure metamorphic rocks. *Tectonophysics* 451, 225-241.

635 Guillot, S., Replumaz, A., Hattori, K., Strzeczynski, P., 2007. Initial geometry of western Himalaya and  
636 ultrahigh pressure metamorphic evolution. *Journal of Asian Earth Sciences* 30, 557-564.

637 Guiraud, M., 1982. *Géothermométrie du faciés schistes vert à glaucophane. Modélisation et applications*.  
638 University of Montpellier. Ph.D.

639 Guiraud, M., Powell, R., Rebay, G., 2001. H<sub>2</sub>O in metamorphism and unexpected behavior in the  
640 preservation of metamorphic mineral assemblages. *Journal of Metamorphic Geology* 19, 445-454.

641 Hacker, B.R., 2008. H<sub>2</sub>O subduction beyond arcs. *Geochemistry Geophysics Geosystems* 9. B03204.

642 Hacker, B.R., Abers, G. A., Peacock, S. M., 2003. Subduction factory 1. Theoretical mineralogy, densities,  
643 seismic wave speeds, and H<sub>2</sub>O contents. *Journal of Geophysical Research* 108, 2029.

644 Hirsch, D.M., Ketchum, R.A., Carlson, W.D., 2000. An evaluation of spatial correlation functions in textural  
645 analysis of metamorphic rocks. *Geological Material Research* 2, 1-21.

646 Holland, T., Baker, J., Powell, R., 1998. Mixing properties and activity-composition relationships of chlorites  
647 in the system MgO-FeO-Al<sub>2</sub>O<sub>3</sub>-SiO<sub>2</sub>-H<sub>2</sub>O. *European Journal of Mineralogy* 10, 395-406.

648 Holland, T.J.B., Powell, R., 1998. An internally consistent thermodynamic dataset for phases of petrological  
649 interest. *Journal of Metamorphic Geology* 16, 309-343.

650 Honegger, K., Le Fort, P., Mascle, G., Zimmerman, J.L., 1989. The blueschists along the Indus Suture zone in  
651 Ladakh, NW Himalaya. *Journal of Metamorphic Geology* 7, 57-72.

652 Jan, M.Q., 1985. High-P rocks along the suture zone around Indo-Pakistan plate and phase chemistry of  
653 blueschists from eastern Ladakh. *Geological Bulletin University of Peshawar* 18, 1-40.

654 Jan, M.Q., 1987. Phase chemistry of blueschists from eastern Ladakh, Himalaya. *Neues Jahrbuch fuer*  
655 *Geologie und Palaeontologie* 10, 613-635.

656 Jarrard, R.D., 2003. Subduction fluxes of water, carbon dioxide, chlorine, and potassium. *Geochemistry*  
657 *Geophysics Geosystems* 4, 8905.

658 Jolivet, L., Faccenna, C., Goffé, B., Burov, E., Agard, P., 2003. Subduction tectonics and exhumation of high-  
659 pressure metamorphic rocks in the Mediterranean orogens. *American Journal of Science* 303, 353-409.

660 Ketcham, R.A., Carlson, W.D., 2012. Numerical simulation of diffusion-controlled nucleation and growth of  
661 porphyroblasts. *Journal of Metamorphic Geology* 30, 489-512.

662 Kim, D., Katayama, I., Michibayashi, K., Tsujimori, T., 2013. Deformation fabrics of natural blueschists and  
663 implications for seismic anisotropy in subducting oceanic crust. *Physics of the Earth and Planetary*  
664 *Interiors* 222, 8-21.

665 Lanari, P., Riel, N., Guillot, S., Vidal, O., Schwartz, S., Pêcher, A., Hattori, K.H., 2013. Deciphering high-  
666 pressure metamorphism in collisional context using microprobe mapping methods: Application to the  
667 Stak eclogitic massif (northwest Himalaya). *Geology* 41, 111-114.

668 Leake, B.F., Woolley, A.R., Arps, C.E.S. et al., 1997. Nomenclature of amphiboles: report of the  
669 subcommittee on amphiboles of the International Mineralogical Association, commission on new  
670 minerals and mineral names. *American Mineralogist* 82, 1019-1037.

671 Lombardo, B., Rolfo, F., 2000. Two contrasting eclogite types in the Himalayas: implications for the  
672 Himalayan orogeny. *Journal of Geodynamics* 30, 37-60.

673 Lopez-Carmona, A., Pitra, P., Abati, J., 2013. Blueschist- facies metapelites from the Malpica-Tui Unit (NW  
674 Iberian Massif): phase equilibria modelling and H<sub>2</sub>O and Fe<sub>2</sub>O<sub>3</sub> influence in high-pressure assemblages.  
675 *Journal of Metamorphic Geology* 31, 263-280.

676 Mahéo, G., Fayoux, C., Guillot, S., Garzanti, E., Capiez, P., Mascle, G., 2006. Geochemistry of ophiolitic rocks  
677 and blueschists from the Sapi-Shergol mélange (Ladakh, NW Himalaya, India): implication for the timing  
678 of the closure of the Neo-Tethys ocean. *Journal of Asian Earth Sciences* 26, 695-707.

679 Martin, L.A.J., Wood, B.J., Turner, S., Rushmer, T., 2011. Experimental measurements of trace element  
680 partitioning between lawsonite, zoisite and fluid and their implication for the composition of arc  
681 magmas. *Journal of Petrology* 52, 1049-1075.

682 Newton, R.C., Charlu, T.V., Kleppa, O.J., 1980. Thermochemistry of the high structural state plagioclases.  
683 *Geochimica and Cosmochimica Acta* 44, 933-941.

684 O'Brien, P.J., Zotov, N., Law, R., Khan, A.M., 2001. Coesite in Himalaya eclogite and implications for models  
685 of India-Asia collision. *Geology* 29, 435-438.

686 Page, F.Z., Armstrong, L.S., Essene, E.J., Mukasa, S.B., 2006. Prograde and retrograde history of the Junction  
687 School eclogite, California, and an evaluation of garnet-phengite-clinopyroxene thermobarometry.  
688 *Contribution to Mineralogy and Petrology* 153, 533-555.

689 Pattison, D.R.M., de Capitani, C., Gaidies, F., 2011. Petrological consequences of variations in metamorphic  
690 reaction affinity. *Journal of Metamorphic Geology* 29, 953-977.



691 Plunder, A., Agard, P., Chopin, C., Pourteau, A., Okay, A.I., 2015. Accretion, underplating and exhumation  
692 along a subduction interface: From subduction initiation to continental subduction (Tavşanlı zone, W.  
693 Turkey). *Lithos* 226, 233-254.

694 Plunder, A., Agard, P., Dubacq, B., Chopin, C., Bellanger, M., 2012. How continuous and precise is the record  
695 of P-T paths? Insights from combined thermobarometry and thermodynamic modelling into subduction  
696 dynamics (Schistes Lustrés, W. Alps). *Journal of Metamorphic Geology* 30, 323-346.

697 Pognante, U., Spencer, D.A., 1991. First report of eclogites from the Himalayan belt, Kaghan valley  
698 (northern Pakistan). *European Journal of Mineralogy* 3, 613-618.

699 Poli, S., Franzolin, E., Fumagalli, P., Crottini, A., 2009. The transport of carbon and hydrogen in subducted  
700 oceanic crust: An experimental study to 5 GPa. *Earth and Planetary Science Letters* 278, 350-360.

701 Poli, S., Schmidt, M.W., 1995. H<sub>2</sub>O transport and release in subduction zones: Experimental constraints on  
702 basaltic and andesitic systems. *Journal of Geophysical Research* 100, 22299-22314.

703 Pouchou, J.L., Pichoir, F., 1988. Determination of mass absorption coefficients for soft X-Rays by use of the  
704 electron microprobe. *Microbeam Analysis*, San Francisco Press, pp 319-324.

705 Ravna, E.J.K., Andersen, B., Jolivet, L., De Capitani, C., 2010. Cold subduction and the formation of lawsonite  
706 eclogite – constraints from prograde evolution of eclogitized pillow lava from Corsica. *Journal of*  
707 *Metamorphic Geology* 28, 381-395.

708 Reuber, I., Colchen, M., Mevel, C., 1987. The geodynamic evolution of the south-Tethyan margin in Zaskar,  
709 NW Himalaya, as revealed by the Spontang ophiolitic mélange. *Geodinamica Acta* 1, 283-296.

710 Robertson, A., 2000. Formation of mélanges in the Indus Suture Zone, Ladakh Himalaya by successive  
711 subduction-related, collisional and post-collisional processes during Late Mesozoic–Late Tertiary time, in:  
712 Khan, M.A., Treolar, P.J., Searle, M.P., Jan, Q. (Eds.), *Tectonics of the Nanga Parbat Syntaxis and the*  
713 *Western Himalaya*. Geological Society of London Special Publication 170, 333-374.

714 Sachan, H.K., Mukherjee, B.K., Ogasawara, Y., Maruyama, S., Ishida, H., Muko, A., Yoshioka, N., 2004.  
715 Discovery of coesite from Indus Suture Zone (ISZ), Ladakh, India: Evidence for deep subduction. *European*  
716 *Journal of Mineralogy* 16, 235-240.

717 Scambelluri, M., Müntener, O., Ottolini, L., Pettke, T., Vannucci, R., 2004. The fate of B, Cl and Li in the  
718 subducted oceanic mantle and in the antigorite breakdown fluids. *Earth and Planetary Science Letters*  
719 222, 217-234.

720 Schumacher, J.C., Brady, J.B., Cheney, J.T., Tonnsen, R.R., 2008. Glaucofane-bearing marbles on Syros,  
721 Greece. *Journal of Petrology* 49, 1667-1686.

722 Shams, F.A., 1972. Glaucofane-bearing rocks from near Topsin, Swat. First record from Pakistan. *Pakistan*  
723 *Journal of Scientific Research* 24, 343-345.

724 Socquet, A., Goffé, B., Pubellier, M., Rangin, C., 2002. Le métamorphisme Tardi-Crétacé à Éocène des zones  
725 internes de la chaîne Indo-Birmane (Myanmar occidentale): Implications géodynamiques. *Comptes Rendus*  
726 *Geoscience* 334, 573-580.

727 Spandler, C., Pirard, C., 2013. Element recycling from subducting slabs to arc crust: A review. *Lithos* 170-  
728 171, 208-223.

729 Sutre, E., 1990. Les formations de la marge nord-neotéthysienne et les mélanges ophiolitiques de la zone  
730 de suture de l'Indus en Himalaya du Ladakh, Inde. PhD Thesis, Poitiers University, France, pp. 662.

731 Tian, Z.L., Wei, C.J., 2014. Coexistence of garnet blueschist and eclogite in South Tianshan, NW China:  
732 dependence of P–T evolution and bulk-rock composition. *Journal of Metamorphic Geology* 32, 743-764.

733 Tsujimori, T., Ernst, W.G., 2014. Lawsonite blueschists and lawsonite eclogites as proxies for palaeo-  
734 subduction zone processes: a review. *Journal of Metamorphic Geology* 32, 437–454.

735 Tsujimori, T., Matsumoto, K., Wakabayashi, J., Liou, J.G., 2006. Franciscan eclogite revisited: re-evaluation  
736 of the P–T evolution of tectonic blocks from Tiburon Peninsula, California, USA. *Mineralogy and*  
737 *Petrology* 88, 243-267.

738 Ukar, E., Cloos, M., 2014. Low-temperature blueschist-facies mafic blocks in the Franciscan melange, San  
739 Simeon, California: Field relations, petrology, and counterclockwise P-T paths. *Geological Society of*  
740 *America Bulletin* 126, 831-856.

741 Ulmer, P., Trommsdorff, V., 1995. Serpentine stability to mantle depths and subduction related  
742 magmatism. *Science* 268, 858-861.

743 Vidal, O., Parra, T., 2000. Exhumation paths of high-pressure metapelites obtained from local equilibria for  
744 chlorite- phengite assemblages. *Geological Journal* 35, 139-161.

745 Viridi, N.S., Thakur, V.C., Kumar, S., 1977. Blueschist facies metamorphism from the Indus suture zone of  
746 Ladakh and its significance. *Himalaya Geology* 7, 479-482.

747 Vitale Brovarone, A., Agard, P., 2013. True metamorphic isograds or tectonically sliced metamorphic  
748 sequence? New high-spatial resolution petrological data for the New Caledonia case study. *Contributions*  
749 *to Mineralogy and Petrology* 166, 451-469.

750 Vitale Brovarone, A., Alard, O., Beyssac, O., Picatto, M., 2014. Lawsonite metasomatism and trace element  
751 recycling in subduction zones. *Journal of Metamorphic Geology* 32, 489-514.

752 Vitale Brovarone, A., Beyssac, O., 2014. Lawsonite metasomatism: A new route for water to the deep Earth.  
753 *Earth and Planetary Science Letters* 393, 275-284.

754 Vitale Brovarone, A., Beyssac, O., Malavieille, J., Molli, G., Beltrando, M., Compagnoni, R., 2013. Stacking  
755 and metamorphism of continuous segments of subducted lithosphere in a high-pressure wedge: The  
756 example of Alpine Corsica (France). *Earth-Science Reviews* 116, 35-56.

757 Vitale Brovarone, A., Groppo, C., Hetenyi, G., Compagnoni, G., Malavieille, J., 2011. Coexistence of  
758 lawsonite-bearing eclogite and blueschist: phase equilibria modelling of Alpine Corsica metabasalts and  
759 petrological evolution of subducting slabs. *Journal of Metamorphic Geology* 29, 583-600.

760 Warren, C.J., Grujic, D., Kellett, D.A., Cottle, J., Jamieson, R.A., Ghalley, K.S., 2011. Probing the depths of the  
761 India-Asia collision: U-Th-Pb monazite chronology of granulites from NW Bhutan. *Tectonics* 30, TC2004.

762 Warren, C.J., Parrish, R.R., Waters, D.J., Searle, M.P., 2005. Dating the geologic history of Oman's Semail  
763 ophiolite: insights from U–Pb geochronology. *Contributions to Mineralogy and Petrology* 150, 403-422.

764 Warren, C.J., Waters, D.J., 2006. Oxidized eclogites and garnet–blueschists from Oman: P–T path modeling  
765 in the NCFMASHO system. *Journal of Metamorphic Geology* 24, 783-802.

766 Waters, D.J., Lovegrove, D.P., 2002. Assessing the extent of disequilibrium and overstepping of prograde  
767 metamorphic reactions in metapelites from the Bushveld Complex aureole, South Africa. *Journal of*  
768 *Metamorphic Geology* 20, 135-149.

769 Wei, C.J., Clarke, G.L., 2011. Calculated phase equilibria for MORB compositions: a reappraisal of the  
770 metamorphic evolution of lawsonite eclogite. *Journal of Metamorphic Geology* 29, 939-952.

771 Yamato, P., Agard, P., Burov, E., Le Pourhiet, L., Jolivet, L., Tiberi, C., 2007. Burial and exhumation in a  
772 subduction wedge: mutual constraints from thermo-mechanical modeling and natural P-T-t data  
773 (Schistes Lustrés, W. Alps). *Journal of Geophysical Research* 112, B07410.

774 Zack, T., Rivers, T., Brumm, R., Kronz, A., 2004. Cold subduction of oceanic crust: Implications from a  
775 lawsonite eclogite from the Dominican Republic. *European Journal of Mineralogy* 16, 909-916.

776

777 **Figure captions**

778 **Fig. 1** – Geological sketch map of the studied area (modified after Honegger et al., 1989). (1) Dras-Naktul  
779 volcanoclastics and flysch; (2) pillow lavas, sill and dyke series; (3) ultramafic lenses; (4) Shergol  
780 conglomerate; (5) mèlange formation; (6) blueschist zone; (7) Karamba and Lamayuru unit; (8) Zanskar unit.  
781 Star: samples location. Inset: simplified tectonic map of the Himalayan orogen showing the locations of the  
782 blueschist facies rocks in the Indus Tsangpo suture zone (ITS). 1, Shangla; 2, Sapi-Shergol; 3, Zildat; 4, Sans  
783 Sang; 5, Yamdrock; 6, Nagaland. Other abbreviations used: NP, Nanga Parbat; NB, Namche Barwa; MBT,  
784 Main Boundary Thrust; MFT, Main Frontal Thrust.

785  
786 **Fig. 2** – (a) Panoramic view of the Sapi-Shergol Ophiolite Melange (in blue). View looking north-westward.  
787 Landscape width is about 20 km. (b,c) Outcrop appearance of the most abundant blueschist lithologies in  
788 the SSOM: volcanoclastic rocks (b) and metabasic rocks (c). (d-g) Representative microstructures of  
789 volcanoclastic (d) and metabasic (e) rocks and of silicic (f) and carbonatic (g) metasediments. The dotted  
790 white line in (d) separates a pluri-mm clast (lower right) from the reddish matrix (upper left). The inset in  
791 (g) shows a detail of a large poikiloblast of calcite including idioblastic lawsonite. Plane Polarized Light (PPL).  
792

793 **Fig. 3** - Processed major elements  $\mu$ -XRF maps of the whole thin sections of samples 14-4B and 14-6F. The  
794 unprocessed  $\mu$ -XRF maps for each element are reported in Fig. SM1 and SM2.

795  
796 **Fig. 4** – Representative microstructures of sample 14-4B. (a) Detail of a discontinuous quartz-rich layer  
797 alternated to thicker lawsonite + phengite + glaucophane layers. Note the small dark garnet on the right.  
798 (PPL). (b, c) Detail of a phengite + lawsonite + glaucophane layer: phengite and glaucophane define the  
799 main foliation. PPL (b) and Crossed Polarized Light (XPL) (c).

800  
801 **Fig. 5** – Representative microstructures of sample 14-6F/G. (a) The main foliation, defined by the preferred  
802 orientation of glaucophane and minor phengite, is overgrown by large lawsonite and garnet porphyroblasts  
803 and is intensely crenulated. PPL (a), XPL (b). (c) Detail of a boudinated lawsonite porphyroblast overgrowing  
804 the fine-grained glaucophane + phengite matrix. Lawsonite and quartz occur in the pressure shadows. Note  
805 the garnet porphyroblasts, overgrowing the main foliation and included in lawsonite. PPL. (d) Detail of a  
806 lawsonite porphyroblast including several garnet crystals, crosscut by thin quartz veins. PPL. (e) Processed  
807 X-ray map of garnet reported in (d), highlighting the inclusion distribution within garnet and its chemical  
808 zoning. (f) Back-scattered (BSE) image of a garnet porphyroblast, showing the distribution of inclusions.  
809 Note the occurrence of a small omphacite inclusion in garnet rim and of a small epidote inclusion in garnet  
810 mantle.

811  
812 **Fig. 6** - Compositional diagrams for the main mineral phases analysed in samples 14-4B and 14-6F/G. (a)  
813 Garnet compositions plotted in the Grs-(Sps+Andr)-(Alm+Prp) diagram. (b) Fe, Mg and Mn X-ray maps of  
814 the same garnet reported in Fig. 3d, e. (c) Omphacite compositions (inclusions in garnet) plotted in the Jd-  
815 Quad-Aeg diagram. (d) Phengite compositions plotted in the Si vs. (Mg + Fe) (a.p.f.u.) diagram. The black  
816 line represents the ideal celadonitic substitution. (e,f) Na-Amphibole compositions plotted in the Si  
817 (a.p.f.u.) vs. Mg/(Mg+Fe<sup>+2</sup>) (e), Si (a.p.f.u.) vs. Na/(Na+Ca) and Si (a.p.f.u.) vs. Fe<sup>+3</sup>/Fe<sub>tot</sub> (f). (g) Ca-Amphibole  
818 compositions plotted in the Si (a.p.f.u.) vs. Mg/(Mg+Fe<sup>+2</sup>).

819  
820 **Fig. 7** – Metamorphic evolution inferred for samples 14-4B and 14-6F. Sm is the main foliation.

821

822 **Fig. 8** – (a) P-T pseudosection calculated for sample 14-4B in the MnNKCFMASH model system and at H<sub>2</sub>O  
823 saturated conditions using the whole rock bulk composition. The variance of the fields varies from two (i.e.  
824 8 phases, white fields) to five (i.e. 5 phases, darker grey fields). Garnet compositional isopleths are reported  
825 for garnet core, mantle and rim in dark, medium and light red, respectively (Alm: dashed; Grs: continuous;  
826 Prp: dotted; Sps: dashed-dotted lines); phengite compositional isopleths are reported in yellow. The  
827 modeled peak assemblage is reported in bold. The black arrow is the prograde portion of the P-T path  
828 inferred from the pseudosection. The entire set of garnet compositional isopleths is reported in Fig. SM3.  
829 (b, c) Same pseudosection of (a), contoured for lawsonite (b) and garnet (c) modal amount (vol%). Note  
830 that lawsonite is predicted to be slightly consumed along the inferred P-T path, whereas garnet is predicted  
831 to increase in modal amount.

832  
833 **Fig. 9** – (a) P-T pseudosections calculated for sample 14-6F in the MnNKCFMASH model system and at H<sub>2</sub>O  
834 saturated conditions using the whole-rock (unfractionated: lower left) and the fractionated (upper right)  
835 bulk compositions, respectively, and used to model the growth of garnet core and mantle (unfractionated  
836 bulk) and garnet rim (fractionated bulk). The variance of the fields varies from two (i.e. 8 phases, white  
837 fields) to four (i.e. 6 phases, darker grey fields). Garnet compositional isopleths are reported for garnet  
838 core, mantle and rim in dark, medium and light red, respectively (Alm: dashed; Grs: continuous; Prp:  
839 dotted; Sps: dashed-dotted lines); phengite compositional isopleths are reported in yellow. The black  
840 arrows are the prograde portions of the P-T path inferred for the growth of garnet core, mantle and rim.  
841 The entire set of garnet compositional isopleths is reported in Fig. SM4. (b, c) Same pseudosections of (a),  
842 contoured for lawsonite (b) and garnet (c) modal amount (vol%). Note that lawsonite is predicted to be  
843 slightly consumed along the inferred P-T path, whereas garnet is predicted to increase in modal amount.

844  
845 **Fig. 10** – (a, b) P-X(Fe<sub>2</sub>O<sub>3</sub>) and T-X(Fe<sub>2</sub>O<sub>3</sub>) pseudosections calculated for sample 14-4B in the  
846 MnNKCFMASHO model system at T = 420°C and P = 22 kbar, respectively. (c, d) P-X(Fe<sub>2</sub>O<sub>3</sub>) and T-X(Fe<sub>2</sub>O<sub>3</sub>)  
847 pseudosections calculated for sample 14-6F (fractionated bulk composition) the MnNKCFMASHO model  
848 system at T = 470°C and P = 20 kbar, respectively. In all the pseudosections the variance of the fields varies  
849 from two (i.e. 8 phases, white fields) to six (i.e. 5 phases, darker grey fields). Garnet compositional isopleths  
850 are reported for garnet rim in red (Alm: dashed; Grs: continuous; Prp: dotted; Sps: dashed-dotted lines).  
851 The modeled equilibrium assemblages are reported in bold. For both the samples, peak-P conditions  
852 decrease with increasing XFe<sub>2</sub>O<sub>3</sub> ( $\Delta P = 2-3$  kbar for sample 14-4B and  $\Delta P = 1$  kbar for sample 14-6F),  
853 whereas peak-T conditions do not significantly change at variable XFe<sub>2</sub>O<sub>3</sub> values.

854  
855 **Fig. 11** – P/T-X(H<sub>2</sub>O) pseudosection calculated for sample 14-4B in the MnNKCFMASH model system along  
856 two different P/T gradients: gradient A (a) coincides with the P-T path constrained using the P-T  
857 pseudosection calculated with H<sub>2</sub>O in excess (black arrow in Fig. 8a); gradient B (b) is steeper (similar to the  
858 early prograde P-T evolution of Eastern Himalayan blueschists reported in the literature; Ao and Bhowmik.,  
859 2014). The variance of the fields varies from two (i.e. 7 phases, white fields) to five (i.e. 5 phases, darker  
860 grey fields). Garnet compositional isopleths are reported for garnet core and rim in dark and light red,  
861 respectively (Alm: dashed; Grs: continuous; Prp: dotted; Sps: dashed-dotted lines). The observed  
862 equilibrium assemblage is reported in bold. The white dotted lines in both pseudosections represent the  
863 H<sub>2</sub>O-saturation surface and divide the pseudosections in a H<sub>2</sub>O-saturated part on the right and in a H<sub>2</sub>O-  
864 undersaturated part on the left. The intersection of garnet compositional isopleths on the H<sub>2</sub>O-saturation  
865 surface in (a) confirms that garnet growth (with the measured composition) occurred at H<sub>2</sub>O-saturated  
866 conditions; garnet core compositional isopleths do not intersect in (b), thus implying that gradient B is not  
867 compatible with the observed mineral assemblage and compositions.

868

869 **Fig. 12** – (a,b) P/T-X(H<sub>2</sub>O) pseudosections calculated for sample 14-6F in the MnNKCFMASHO model system  
870 along the same gradient A as in Fig. 11a and using the whole-rock (unfractionated: a) and the fractionated  
871 (b) bulk compositions. The variance of the fields varies from two (i.e. 7 phases, white fields) to five (i.e. 5  
872 phases, darker grey fields). Garnet compositional isopleths are reported for garnet core and rim in dark and  
873 light red, respectively (Alm: dashed; Grs: continuous; Prp: dotted; Sps: dashed-dotted lines). The white  
874 dotted line represents the H<sub>2</sub>O-saturation surface and divides the pseudosections in a H<sub>2</sub>O-saturated part  
875 on the right and in a H<sub>2</sub>O-undersaturated part on the left. The intersection of garnet compositional  
876 isopleths on the H<sub>2</sub>O-saturation surface confirms that garnet growth (with the measured composition)  
877 occurred at H<sub>2</sub>O-saturated conditions.(c-f) Same P/T-X(H<sub>2</sub>O) pseudosection of (a, b) contoured for lawsonite  
878 (c, d) and garnet (e, f) modal amounts (in vol%). The red ellipses indicate the P-T-X(H<sub>2</sub>O) conditions inferred  
879 for the growth of garnet core and rim from Fig. 12a, 12b. H<sub>2</sub>O addition is required to form lawsonite (c, d).  
880 A protracted H<sub>2</sub>O influx at high pressure is required in order to allow the contemporaneous growth of  
881 garnet, which requires H<sub>2</sub>O-saturated conditions (e, f) and lawsonite, whose growth subtracts H<sub>2</sub>O to the  
882 system (c, d) (see text for further details).

883

884 **Fig. 13** - (a) P-T path constrained for the Sapi-Shergol blueschist unit (red thick vs. dotted arrows are the P-T  
885 paths constrained in the MnNKCFMASHO vs. MnNKCFMASH system, respectively; the P-T path previously  
886 constrained by Honegger et al., 1989 and Guillot et al., 2008 is reported in orange) compared with the P-T  
887 paths of the other Himalayan blueschist rocks: Shangla (in yellow: Guillot et al., 2008) and Nagaland  
888 Ophiolite Complex (in green: Ao and Bhowmik, 2014). The dashed grey arrow is the schematic P–T path  
889 followed by the sedimentary particles in the accretionary wedge, as resulting from the thermomechanical  
890 numerical study of Yamato et al. (2007). (b) P-T diagram comparing the maximum P-T conditions for well-  
891 documented examples of accretionary terranes in subduction zones (modified from Agard and Vitale  
892 Brovarone, 2013 and Plunder et al., 2015, with references therein) with the P-T conditions experienced by  
893 the Sapi-Shergol blueschist unit (this study; red squares) and the Nagaland Ophiolite Complex of far-eastern  
894 Himalaya (Ao and Bhowmik, 2014; green square). Data are mainly derived from: Agard et al. (2001b),  
895 Plunder et al. (2012): Western Alps; Ravna et al. (2010), Vitale Brovarone et al. (2011, 2013), Agard and  
896 Vitale Brovarone (2013): Corsica; David and Whitney (2008), Plunder et al. (2015): Turkey; Warren et al.  
897 (2005), Warren and Waters (2006), Agard and Vitale Brovarone, (2013): Oman; Agard et al. (2006): Zagros;  
898 Fitzherbert et al. (2003, 2004, 2005), Agard and Vitale Brovarone (2013), Vitale Brovarone and Agard  
899 (2013): New Caledonia; Banno et al. (2000), Page et al. (2006), Tsujimori et al. (2006), Ernst and McLaughlin  
900 (2012), Ukar and Cloos (2014): Franciscan Complex (western USA).

Fig. 1

[Click here to download high resolution image](#)

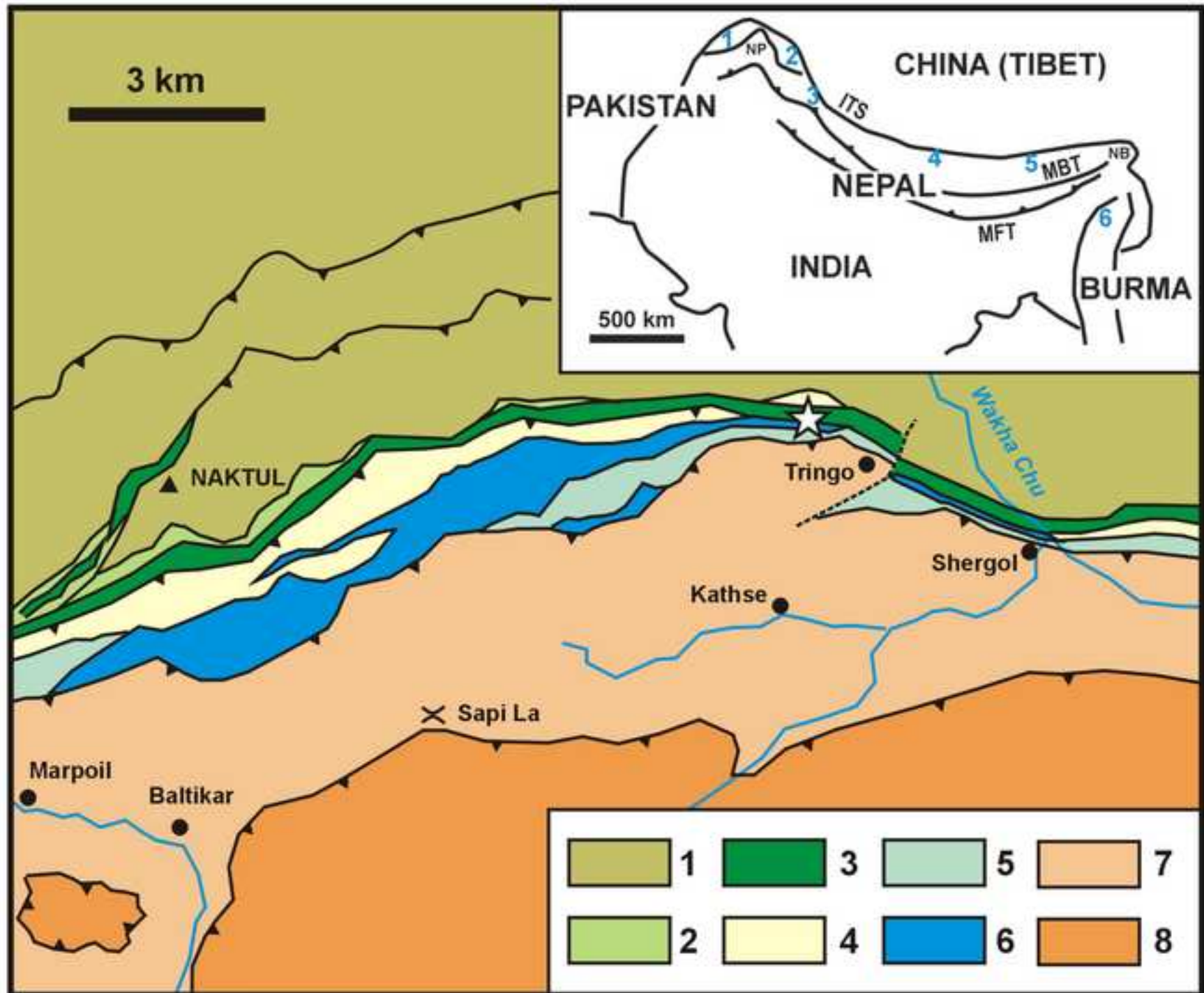


Fig. 2

[Click here to download high resolution image](#)

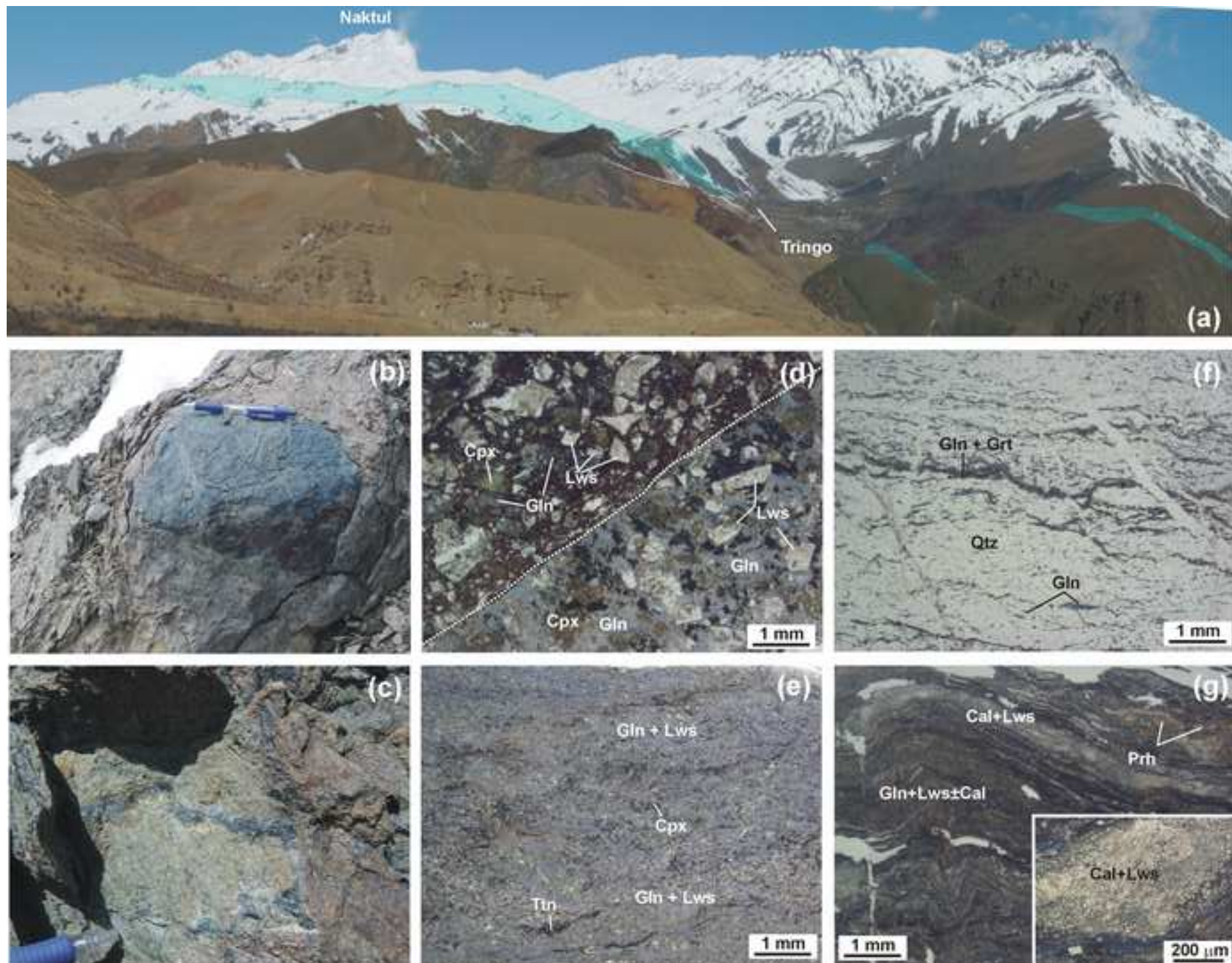


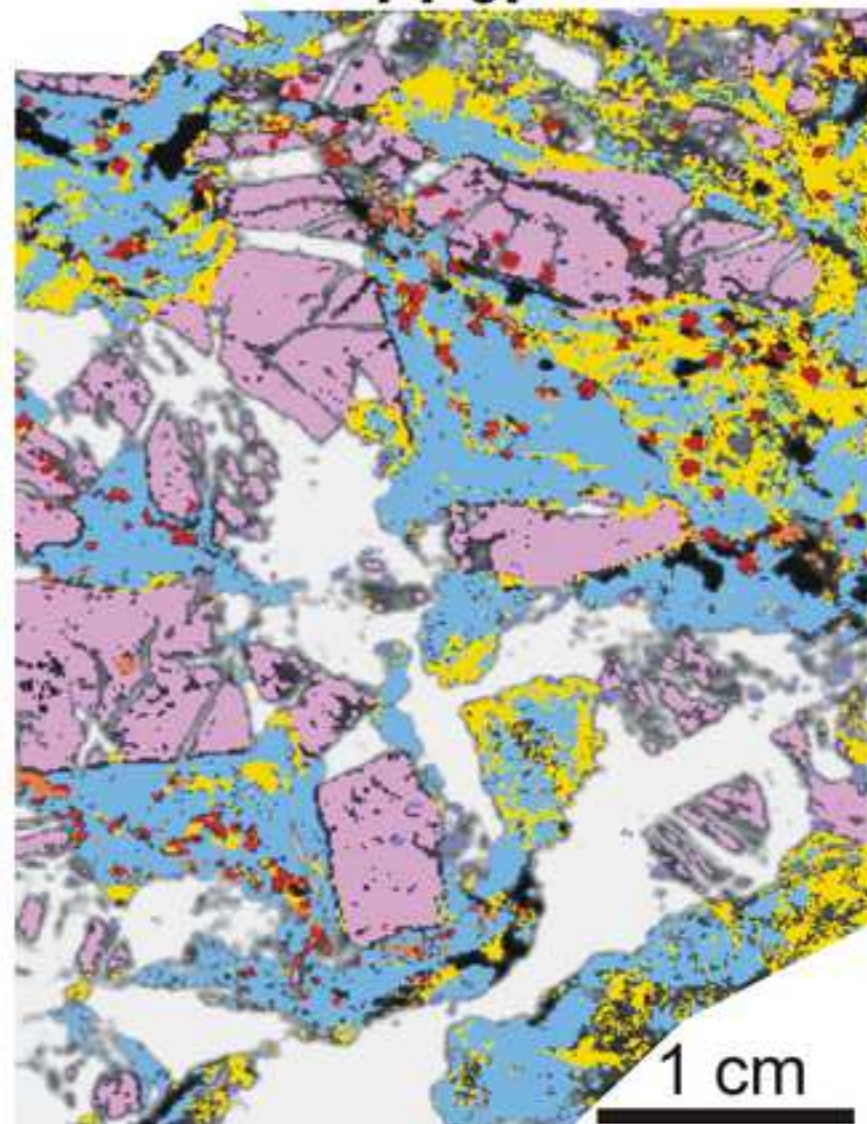
Fig. 3

[Click here to download high resolution image](#)

14-4B



14-6F



Qtz	Lws	Gln	Phe	Ttn
Grt <sub>C</sub>	Grt <sub>R</sub>	Cal	Ab	Ap



Fig. 4

[Click here to download high resolution image](#)

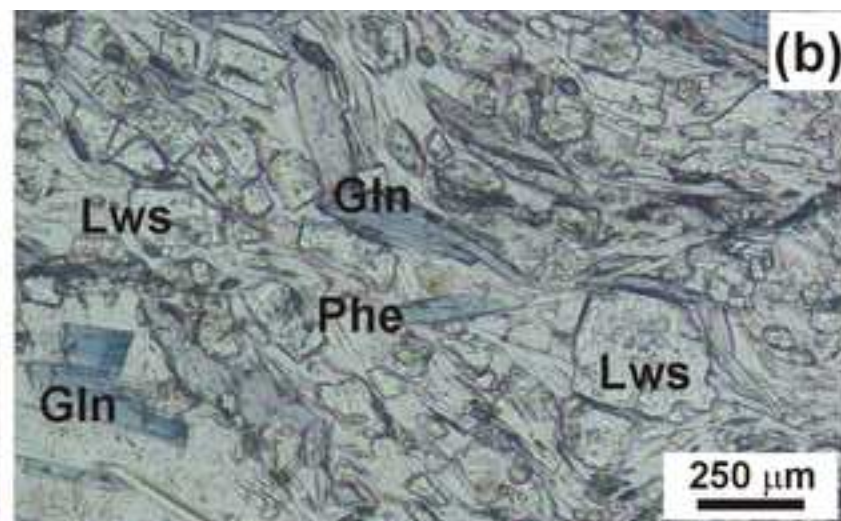
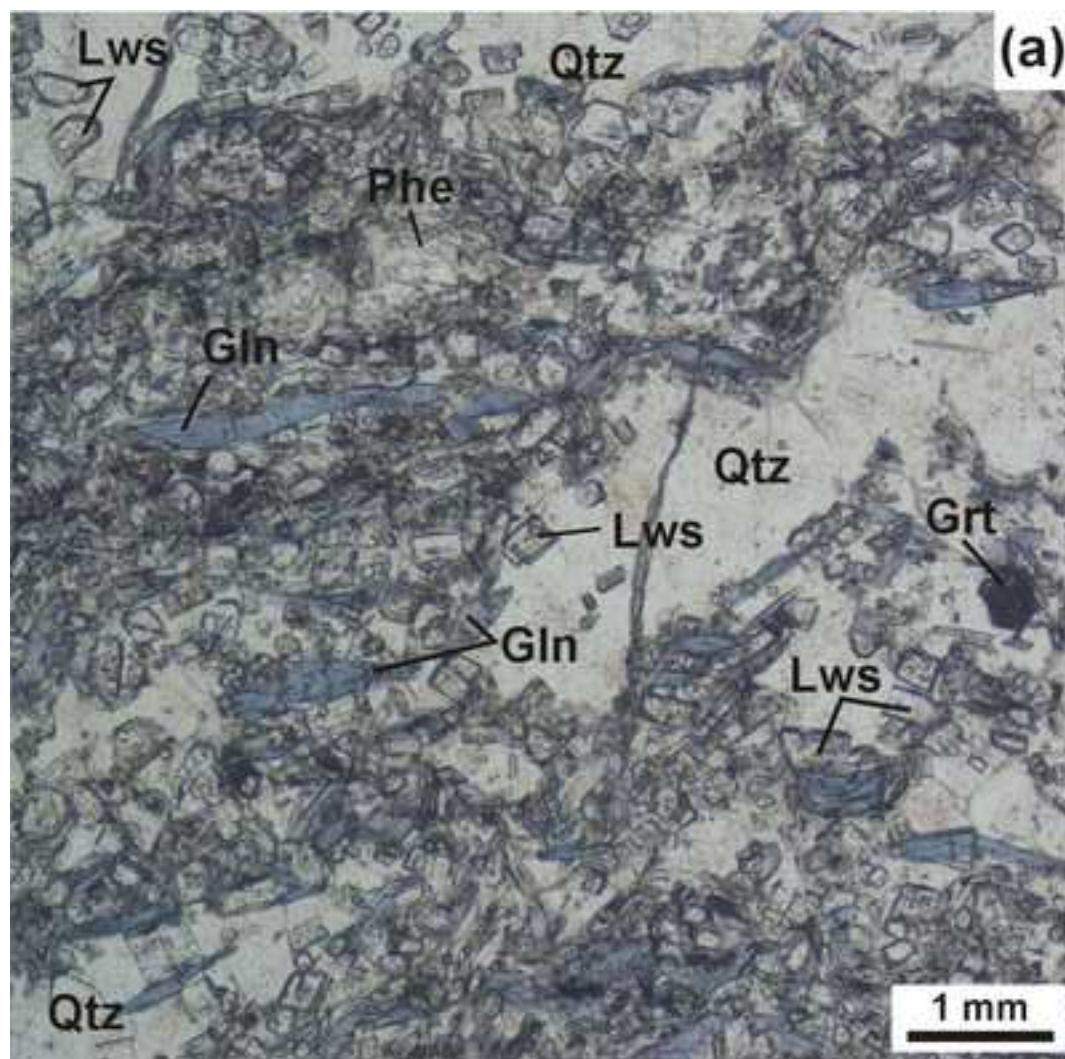


Fig. 5  
[Click here to download high resolution image](#)

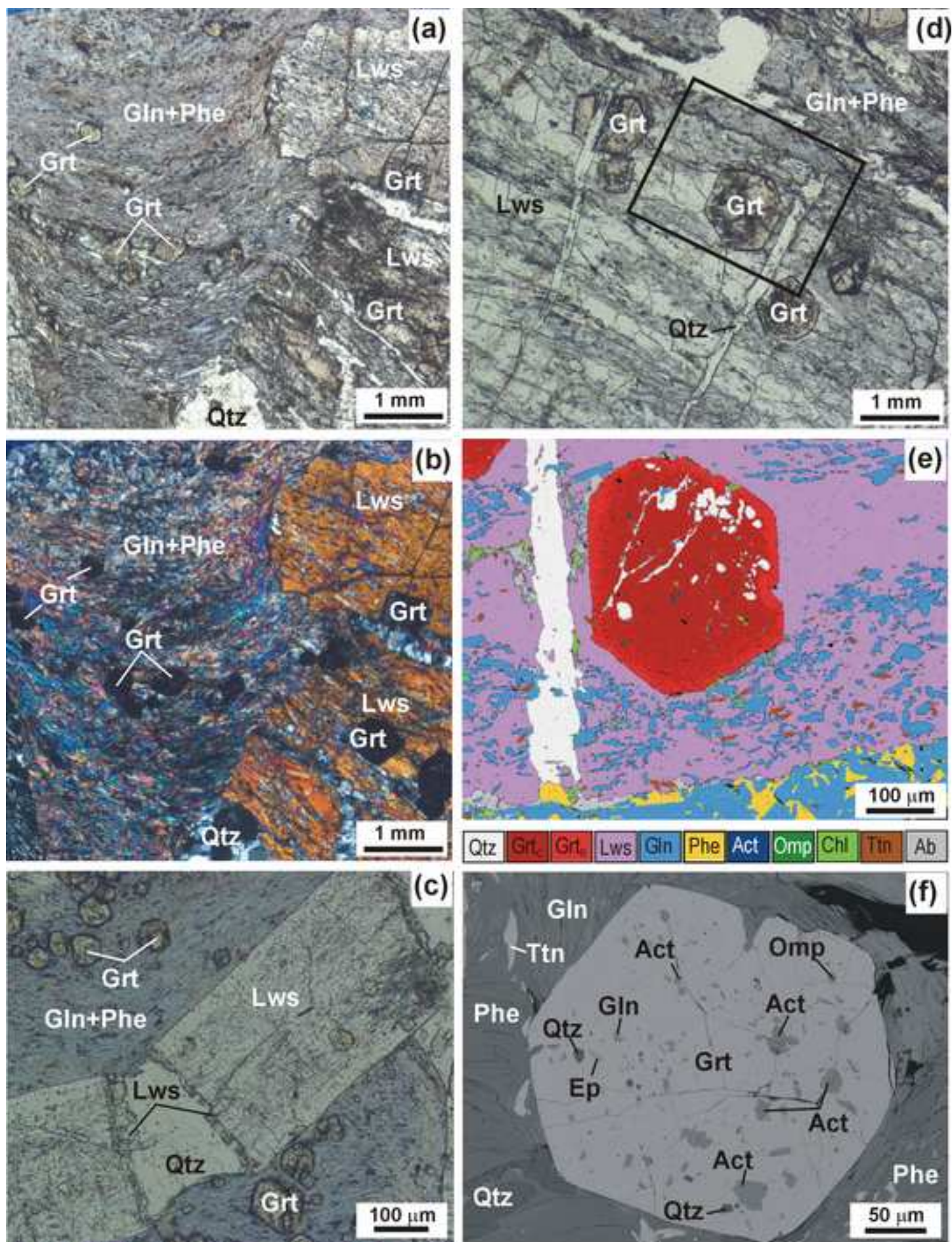


Fig. 6

[Click here to download high resolution image](#)

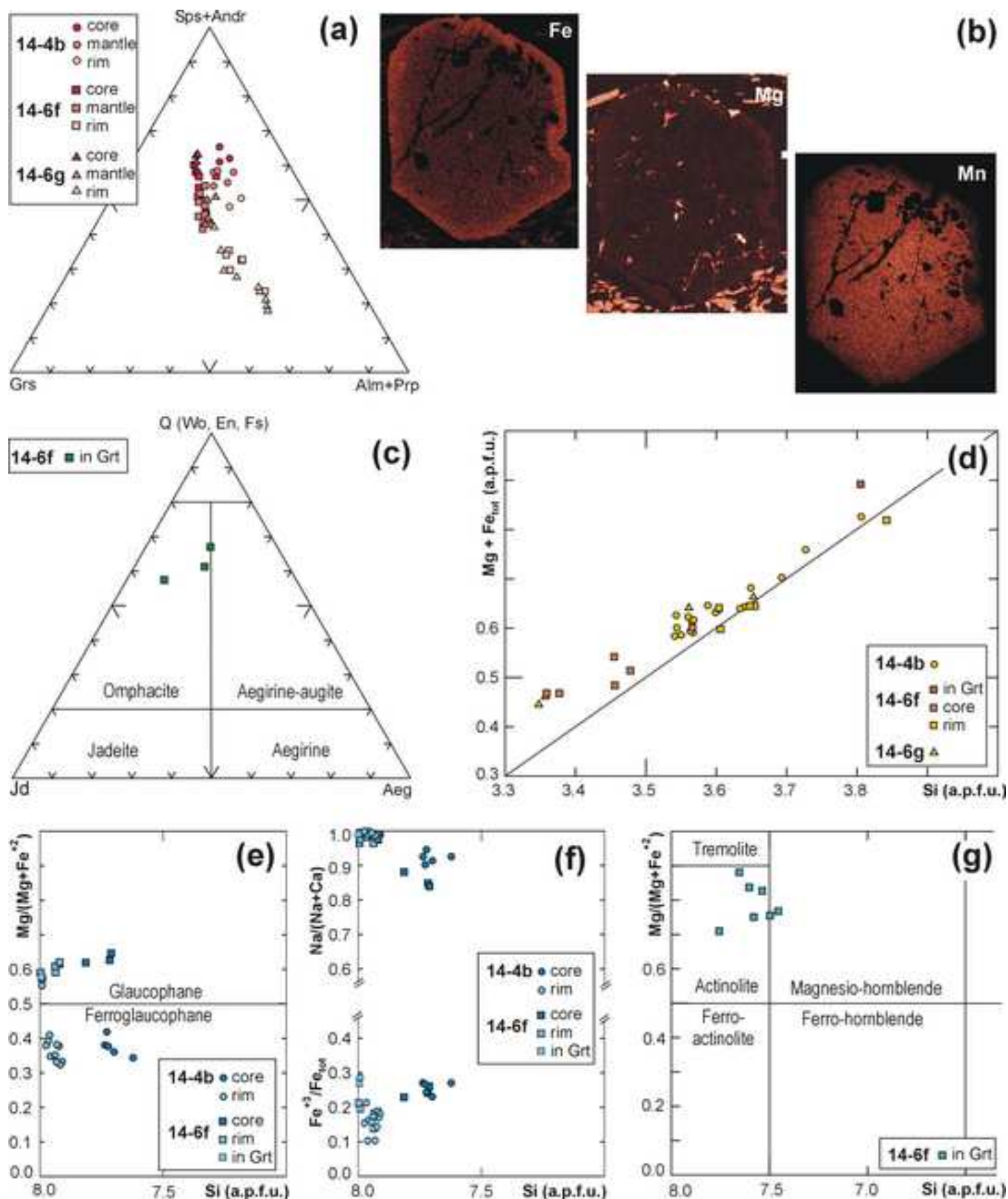
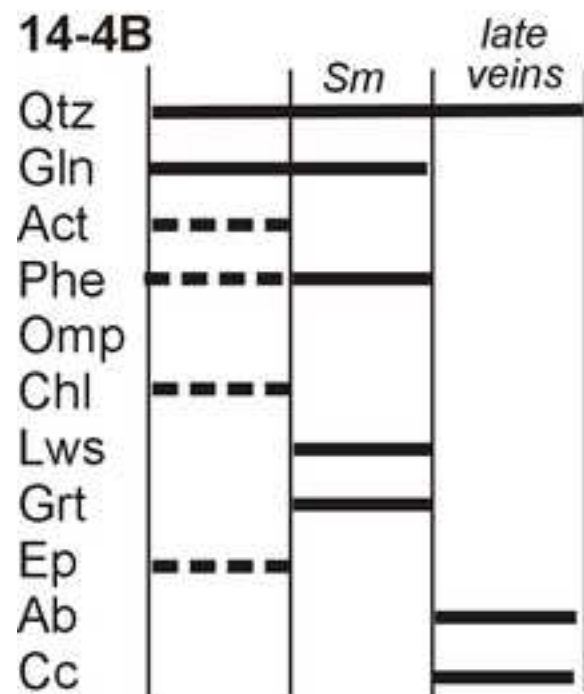


Fig. 7

[Click here to download high resolution image](#)

14-4B



14-6F

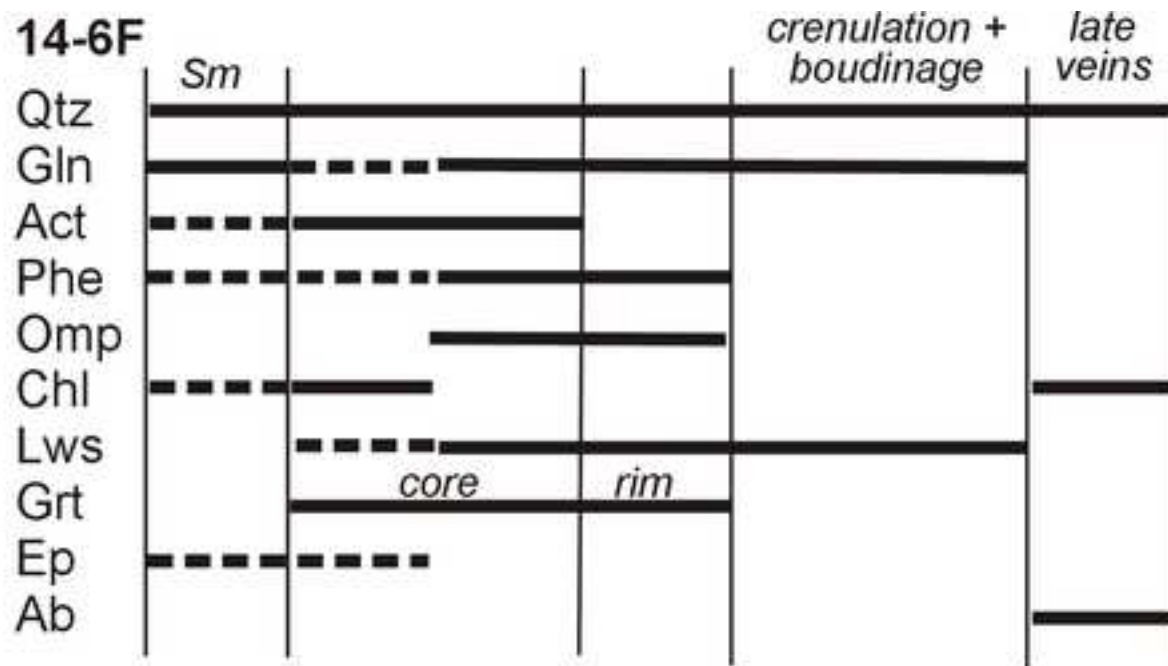


Fig. 8

[Click here to download high resolution image](#)

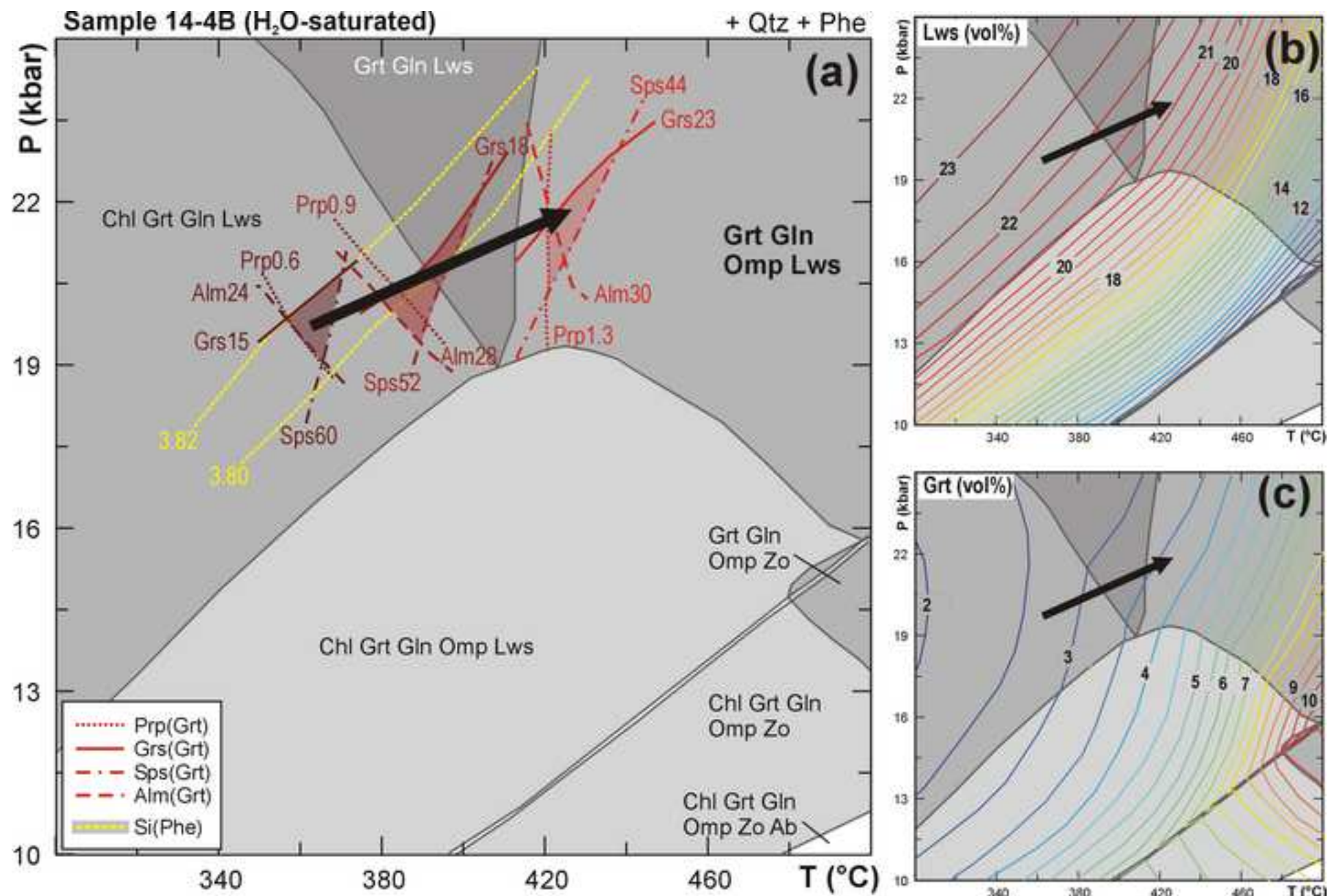


Fig. 9

[Click here to download high resolution image](#)

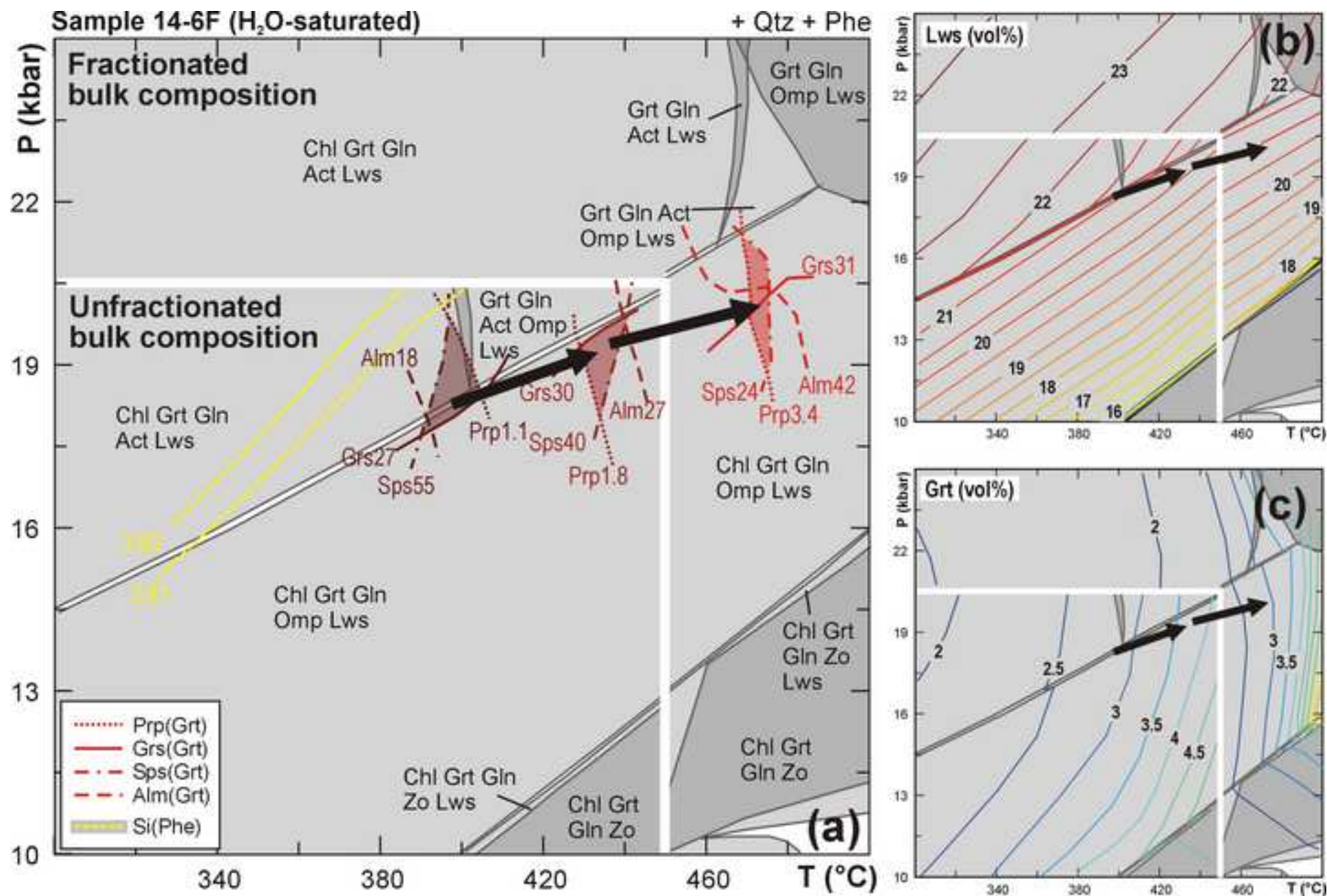


Fig. 10

[Click here to download high resolution image](#)

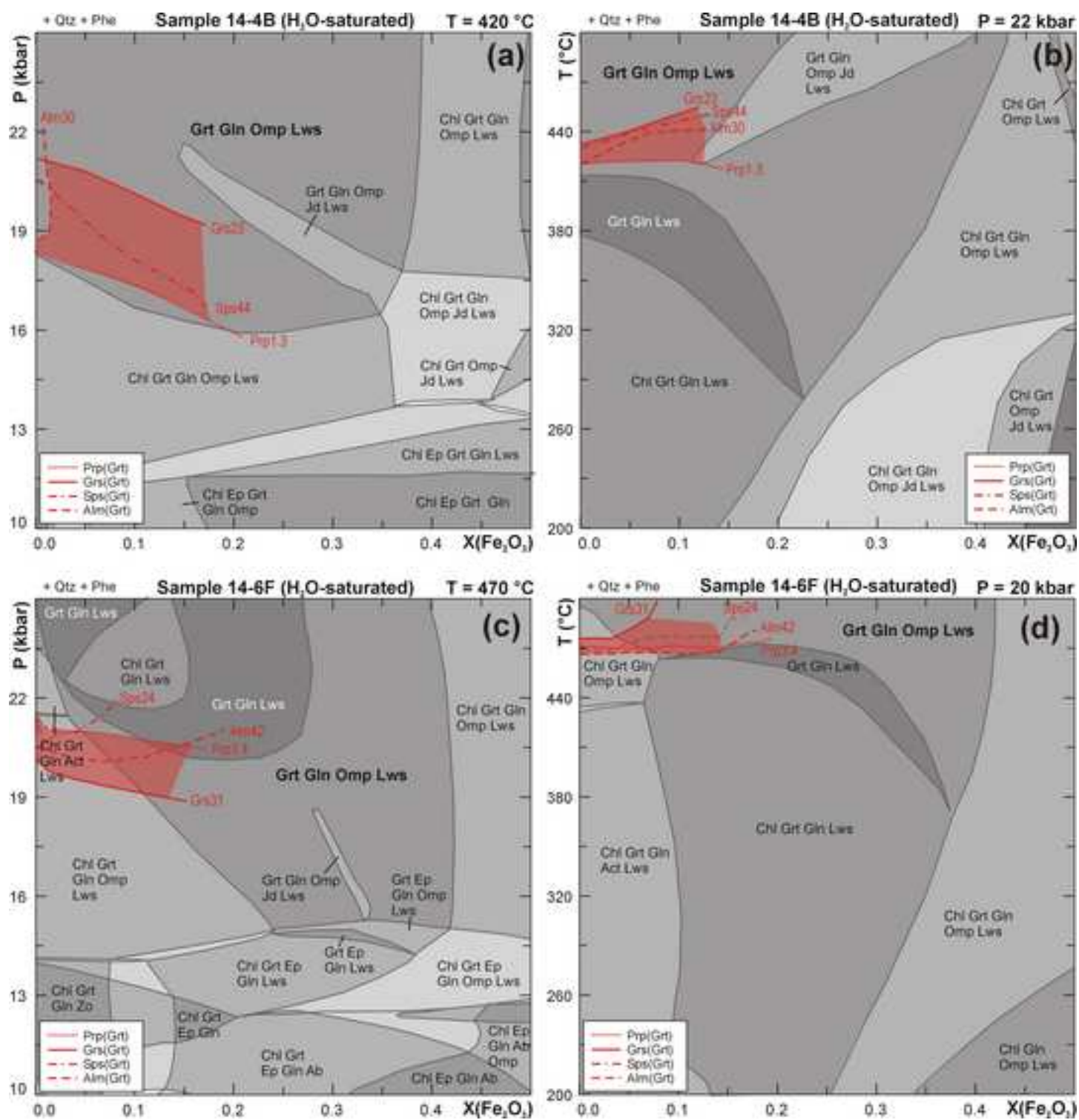
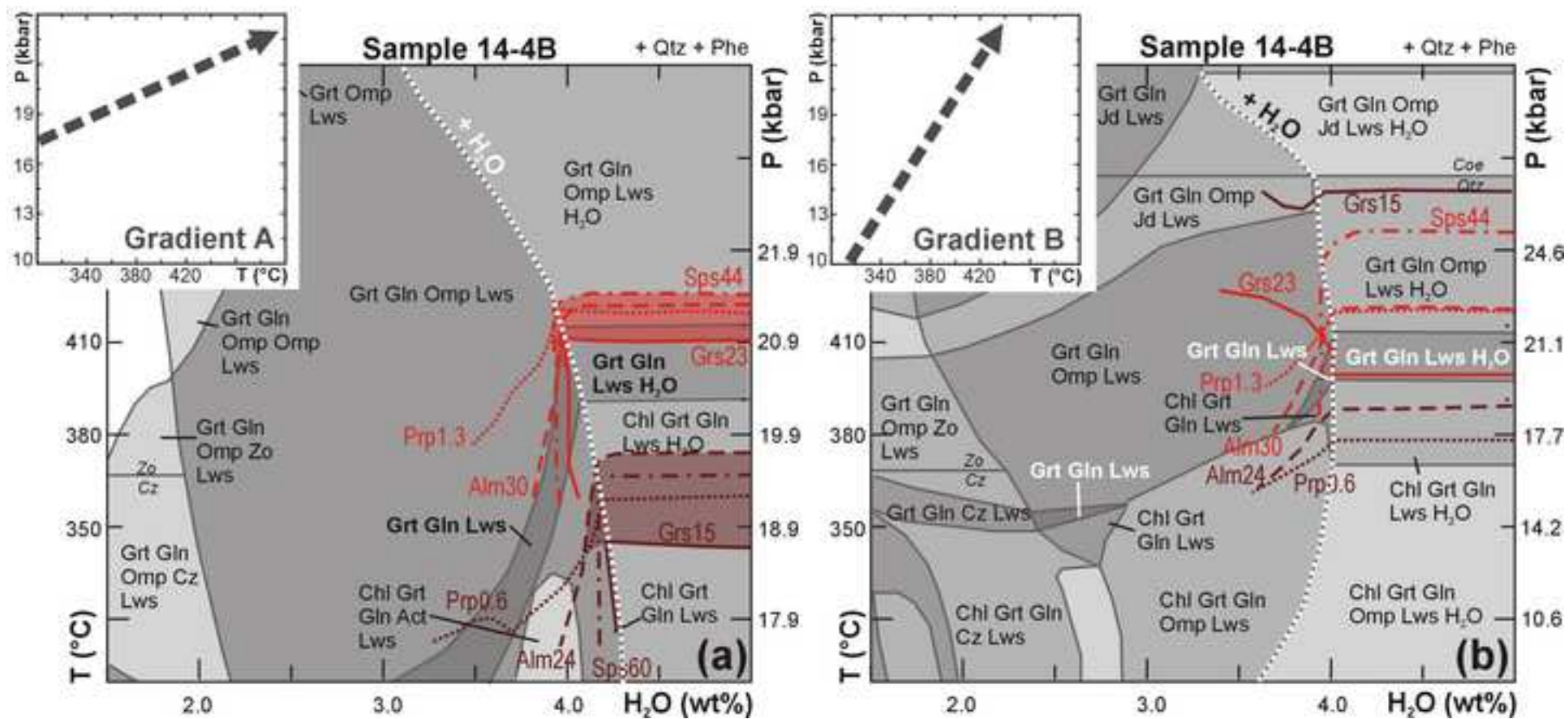


Fig. 11

[Click here to download high resolution image](#)





**Fig. 12**  
[Click here to download high resolution image](#)

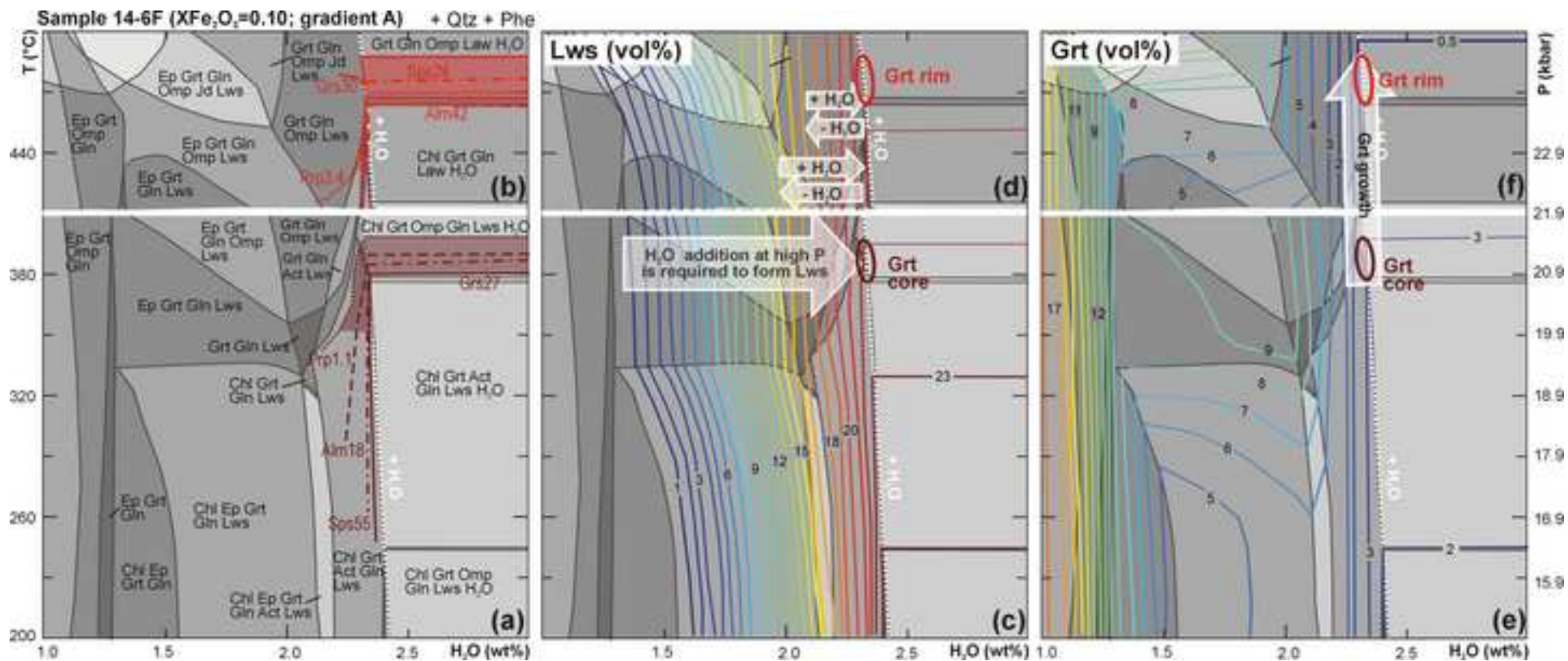
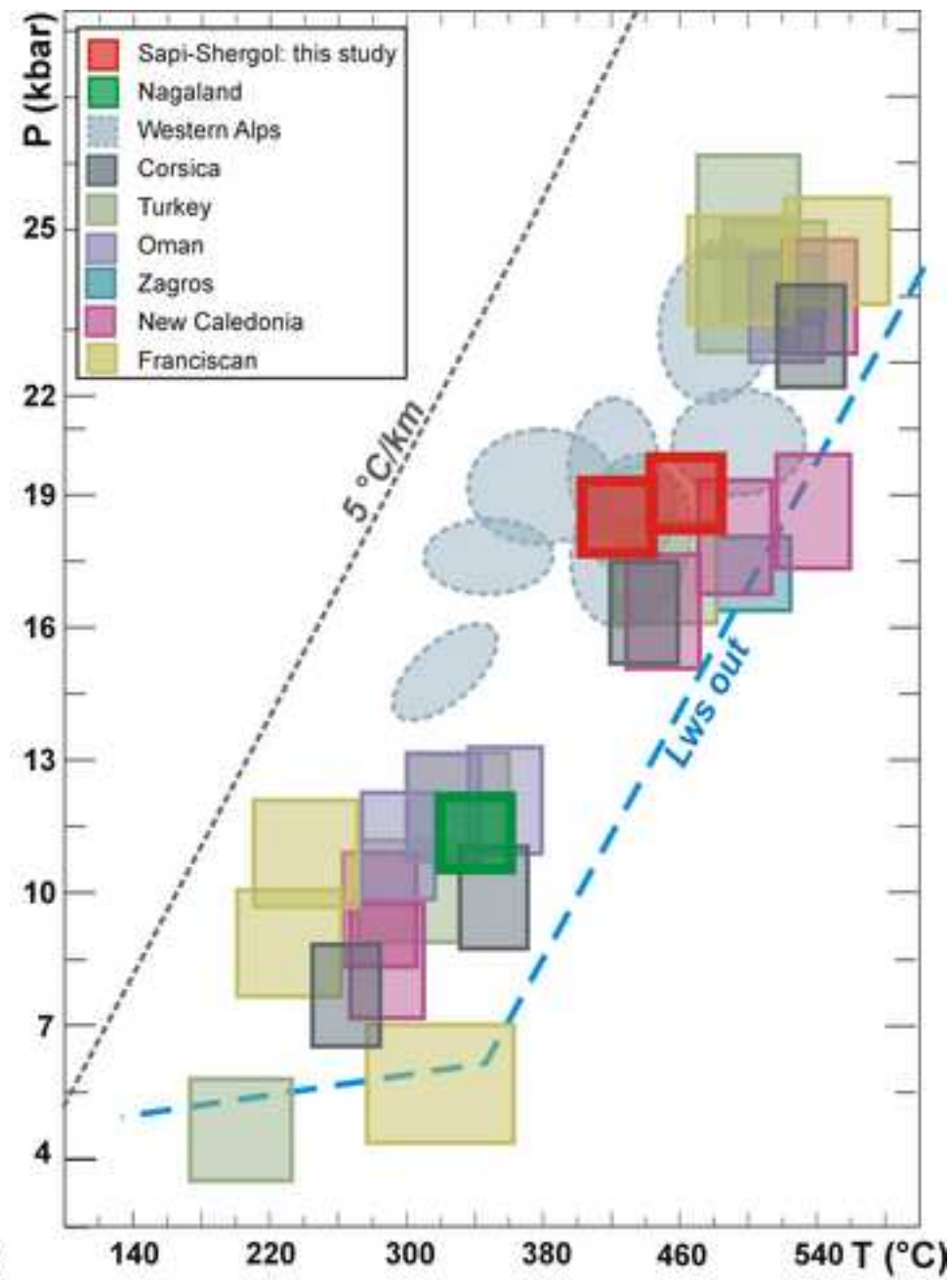
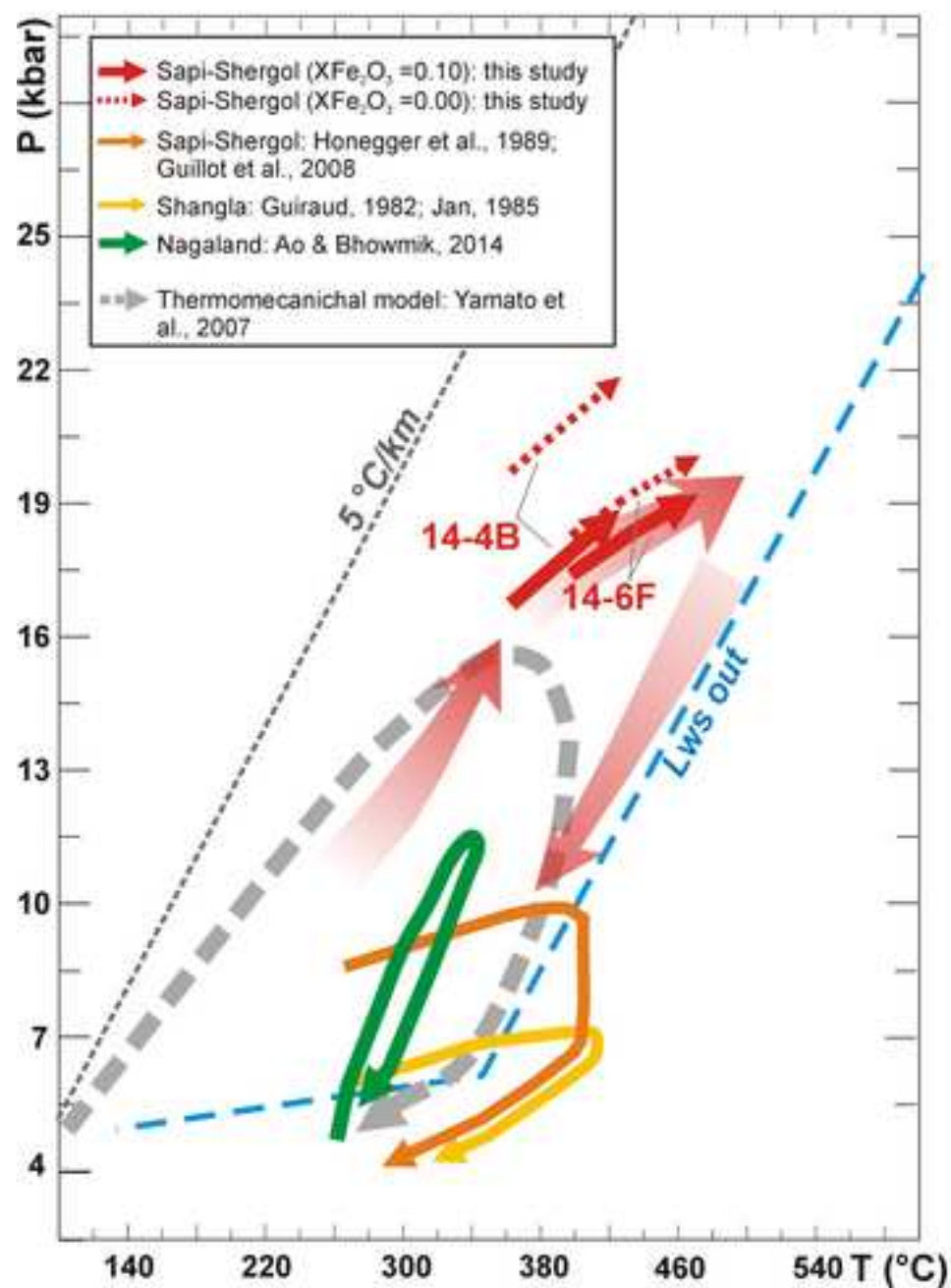


Fig. 13  
[Click here to download high resolution image](#)



**Table 1**[Click here to download Table: Table 1.xlsx](#)**Table 1 - Modal (vol%) and bulk (wt%) compositions of samples 14-4B and 14-6F**

Sample	14-4B	14-6F	
Qtz	42	21	
Lws	21	22	
Phe	22	9	
Gln	12	44	
Grt	3	4	
Total	100	100	

Sample	14-4B	14-6F	
		unfractionated	fractionated
SiO <sub>2</sub>	70.26	61.69	62.91
Al <sub>2</sub> O <sub>3</sub>	14.40	15.76	15.48
FeO	4.20	7.14	7.01
MgO	1.80	4.75	4.96
MnO	1.05	0.93	0.06
CaO	4.66	5.32	4.95
Na <sub>2</sub> O	0.96	3.34	3.51
K <sub>2</sub> O	2.67	1.07	1.12
Total	100.00	100.00	100.00